Article:
Couperthwaite, FK, Thordarson, T, Morgan, DJ orcid.org/0000-0002-7292-2536 et al. (2 more authors) (2020) Diffusion timescales of magmatic processes in the Moinui lava eruption at Mauna Loa, Hawai`i, as inferred from bimodal olivine populations. Journal of Petrology. egaa058. ISSN 0022-3530

https://doi.org/10.1093/petrology/egaa058

Diffusion timescales of magmatic processes in the Moinui lava eruption at Mauna Loa, Hawai`i, as inferred from bimodal olivine populations

[1]Couperthwaite, F. K., Institute of Geophysics and Tectonics, School of Earth and Environment, University of Leeds, Leeds, UK, LS2 9JT.

Corresponding author: eefkc@leeds.ac.uk, +61435370082

[2]Thordarson, T., Faculty of Earth Sciences, University of Iceland, Sturlugarta 7, 101 Reykjavík, Iceland

[1]Morgan, D. J., Institute of Geophysics and Tectonics, School of Earth and Environment, University of Leeds, Leeds, LS2 9JT, UK

[1]Harvey, J., Institute of Geophysics and Tectonics, School of Earth and Environment, University of Leeds, Leeds, LS2 9JT, UK

[1]Wilson, M., Institute of Geophysics and Tectonics, School of Earth and Environment, University of Leeds, Leeds, LS2 9JT, UK

Current affiliation [1]Couperthwaite, F.K. College of Earth, Ocean and Atmospheric Sciences, Oregon State University, Oregon, USA, 97330

ABSTRACT

The 2.1 ka Moinui lava flow field, erupted from the southwest rift zone of Mauna Loa, Hawai`i, exhibits striking textural and geochemical variations, that can be used to interpret magma processes pre-, syn- and post-eruption. From this lava flow, the duration of magma storage and storage conditions, the timescales over which magma is transported to the surface, and flow emplacement mechanisms at Mauna Loa are determined. Electron microprobe analysis (EMPA) and diffusion chronometry of olivine crystals identify two distinct crystal populations: a primitive, polyhedral olivine population with core compositions of Fo_{90-88} and a more evolved, platy olivine population with core compositions of Fo_{83-82}. Fe-Mg diffusion modelling of these olivine populations gives distinct timescales for each population; platy olivines yield timescales of days up to a few weeks, while polyhedral olivines yield timescales of months to years. Despite the nature of a well-insulated pāhoehoe flow, meaning that post-emplacement diffusion continues for some time, a wealth of time information can be retrieved concerning pre-eruptive magmatic processes as well as the processes associated with the lava extrusion. The short timescales obtained from the platy olivine crystals and the observed equilibrium between its cores and

ambient melt suggest late-stage nucleation and crystal growth in the shallow conduit and during lava emplacement. Conversely, the longer timescales and olivine-melt disequilibrium of the polyhedral olivine crystals suggests accumulation from a deeper source and subsequent transportation to shallow magma storage beneath the summit of Mauna Loa months, or even years before eruption. The chemical and textural details of the Moinui lava reflect the mode of flow emplacement and may have implications for the interpretation of the distribution of spinifex and cumulate olivine within komatiites; high-temperature, low-viscosity lavas, common in the Archean.

Key-words: Fe-Mg diffusion; olivine; Hawai`i; pāhoehoe; komatiite

INTRODUCTION

Eruptions at Mauna Loa volcano, Big Island, Hawai`i, averaged 1 or 2 events every 10 years throughout the 19th and 20th centuries, until it entered a dormant period in 1984 (Lockwood & Lipman, 1987; Rhodes, 1988; Barnard, 1995). Many authors have made magmatism and volcanism at Mauna Loa their topic of research, including models for the crystallisation of the lavas (e.g. Wilkinson & Hensel, 1988; Crisp *et al.*, 1994), evaluations of subaerial and submarine activity (e.g. Garcia *et al.*, 1995; Helz *et al.*, 2014), investigation of geochemical linkages between Mauna Loa and Kīlauea lavas (e.g. Rhodes *et al.*, 1989; Marske *et al.*, 2007) and the nature of the mantle source (e.g. Rhodes & Hart, 1995; Pietrsuzka *et al.*, 2013). A perspective that is under-studied

to date is the study of pre- and syn-eruptive magmatic timescales recorded by crystals carried in magmas. Such timescales unravel details of the timing of magma storage, and the magmatic processes taking place within Mauna Loa prior to an eruption.

The Moinui flow field formed by lava effusion from vents high on Mauna Loa volcano 2,100 years ago (Perring *et al.*, 2004; Trusdell & Lockwood, 2017). It contains two morphologically distinct olivine populations, as identified by Perring *et al.* (2004), where one is polyhedral and the other is platy. The polyhedral olivine crystals have core compositions of Fo_{90-88} and the platy olivines have core compositions of Fo_{83-82}. This study combines field, textural and geochemical data to assess timescales of crustal transport, storage of the olivine crystals and flow emplacement prior to and during the 2.1 ka Moinui eruption.

Field observations are used here to constrain the modes of lava emplacement using the principles outlined in Walker (1991), Hon *et al*. (1994) and Thordarson & Self (1998), whilst scanning electron microscopy (SEM) and electron microprobe analysis of polished lava materials enabled the identification of olivine crystal populations and the constraint of timescales from Fe-Mg inter-diffusion.

GEOLOGICAL SETTING

At nearly 9 km above the floor of the central Pacific (4,167 m above sea level), Mauna Loa is the largest volcano on Earth. Mauna Loa's summit crater Moku`āweoweo

forms an elongate collapse caldera 15 km^2 in area, with two associated rift zones extending to the east-northeast (NERZ) and to the southwest (SWRZ), shown in Fig. 1. The start of written records occurred only around 1780, with the eruption of 1832 routinely listed as Mauna Loa's first "recorded" historical eruption (Barnard, 1995). Eruptions from 1843 to the present began with activity near or within the summit crater, and are followed within a few days by more voluminous flank eruptions (Lockwood & Lipman, 1987). The origin of pre-1843 eruptions is less well-known due to the burial of older flows by younger lavas and due to deep weathering (Lockwood & Lipman, 1987; Trusdell & Lockwood, 2017).

The Moinui lava flow (Fig. 1) extends 32 km westwards from the upper slopes of the SWRZ near the summit between Keokea and Captain Cook (Trusdell & Lockwood, 2017). It is very well exposed in road cuts along Highway 160 near the entrance to Pu`uhonua o Hōnaunau State Park and along Highway 11 just north of Keokea.

METHODS

Field sampling considering flow morphology and structure

The Moinui samples were collected from a 50 m long road cut along Highway 160, between Grid Reference 0194285E 2150759N and Grid Reference 0194322E 2150721N (UTM Zone 5Q), featured in Fig. 2.

Fig. 2(a) shows a sheet lobe (labelled L1) that features the central domain of an elongate tumulus, corresponding to an internal magma pathway at the time of lava emplacement. The pāhoehoe lobes (L2a-L4) stacked on top of the L1 flanks were most likely formed as sideways breakouts from either side of the tumulus ridge (i.e. the pathway). This deduction is supported by the observation that lobe L2a extends from within an inflation cleft on the right side and near the base of the elongate tumulus (circled).

The road cut was split into 3 sections for systematic sampling, Section 1 (GR 0194304E, 2150744N), Section 2 (GR 0194302E, 2150743N) and Section 3 (GR 0194322E 2150721N). The outcrops vary in thickness from 1.5 to ~3 m and comprise multiple units, referred to here as lava lobes (e.g. Self *et al.*, 1998; Fig. 2). The lobes consist of upper crust, lava core (the central part of the lobe) and basal crust as defined in Thordarson & Self (1998) where the upper crust and basal crust are more vesiculated than the dense interior (Aubele *et al.*, 1988). These are labelled (green) in Figures 2(a)-(b) and described in Fig. 2 (c) where the lava core represents the molten lava during the lobe emplacement and the vesicular upper crust and basal crust are the crust that formed as the lobe developed. These distinctions form the basis of our sampling strategy. We collected four sets of samples from 3 lobes (M1-M4 where M2 is from the thinner tapered edge of M1) within the 3 sections; where each set included a sample from the vesicular upper crust (labelled TC and then a number), the lava core (CL) and basal crust (BC). The samples were cut into standard sections and polished

up to Syton® colloidal silica grade for a defect-free polish for electron-backscatter diffraction (EBSD) analysis.

Analytical and Modelling Methods

Electron Microprobe Analysis (EPMA)

Compositional traverses from olivine rims to cores were measured on the JEOL JXA8230 EMPA at the University of Leeds. Compositions of the full traverses can be found in the Supplementary Data. The length of the profile extracted was dependent on the apparent diffusion width. Spot sizes of 5 μm were used at 5-10 μm intervals for profile lengths less than 150 μm, with the spot closest to the crystal rim measured ~5 μm from the edge of the crystal. The spot interval was increased to 10-20 μm for profile lengths over 150 μm, for efficiency. The EMPA analytical conditions included an accelerating voltage of 20 kV and a beam current of 30-40 nA. Five wavelength-dispersive spectrometers were used for analysis with varying on-peak count times over multiple runs of 90-100 s for Ca, 30-60 s for Al, Ni and Mn, 20-40 s for Si, Mg and Fe and 1530 s for Cr. Off-peak count times were half that of the on-peak count times. Most analyses returned totals in the range 98.4-101.1 wt. %. Analyses outside this range were rejected. Mineral standards obtained from the Smithsonian Institute, Washington D.C. were used to calibrate the EMPA (Jarosewich, 1980).

Primary standards and detection limits are reported in the Supplementary Data. Repeat analyses of the San Carlos olivine standard (NMNH 111312-44) over

multiple runs were used to estimate the accuracy and reproducibility of forsterite (Fo = (Mg/Mg+Fe)*100). The Fo content of the San Carlos olivine was determined with a precision of 2σ = 0.1-0.2 mol. % (n=84 over the course of the study).

Scanning Electron Microscope and Electron Backscatter Diffraction (EBSD)

High resolution backscattered electron (BSE) images of the polyhedral and platy olivines were collected for both thin section navigation purposes and for compositional calibration for diffusion modelling, using the FEI Quanta 650 Field Emission Gun-Environmental Scanning Electron Microscope (FEGSEM) at the University of Leeds. The machine was operated at aperture 4, with a spot size of 5 μm and voltage of 20 kV.

The FEI Quanta 650 FEGSEM was also used to analyse the orientation of the crystallographic axes of the olivine crystals using EBSD. These EBSD data were processed using Oxford Instruments *Channel 5* software to calculate and constrain the angles between crystallographic axes and the measured compositional traverses, when processing the diffusion anisotropy (cf. Costa & Chakraborty, 2004). Diffusion along the [001] crystallographic orientation is around 6 times faster than along [100] or [010] (Nakamura & Schmalzried, 1983; Dohmen & Chakraborty, 2007a and b; Dohmen *et al*, 2007), so it is essential to know the orientation of the crystal relative to the compositional traverse when processing the diffusion anisotropy.

X-ray fluorescence (XRF)

Bulk-rock major element analyses were determined by x-ray fluorescence (XRF) at Origin Analytics, Welshpool using a 4KW Bruker S4 WD-XRF instrument. Around 10 g of homogenised powders were analysed from the basal crust, lava core and upper crust of sample M1. Samples were prepared as fused disks using a Claisse M4 fusion instrument; 0.5000 g $\pm$ 0.0005 g of sample was combined with 7.5000 g $\pm$ 0.0005 g of flux (50:50 mix of $Li_2B_4O_7$:$LiBO_2$) and fused using the Claisse default program 3 before being poured into 32 mm casting dishes. The machine was calibrated using 25 geological reference materials prepared in an identical manner to the samples. Drift was monitored using the Ausmon drift correction standard (XRF Scientific Ltd) and corrected within the instrument software. Loss on ignition was determined gravimetrically on a separate powder aliquot after heating to 1025 °C.

Thermometry and Oxygen Fugacity

Equilibration temperatures for these samples was calculated using matrix glass compositions that were measured using EMPA with a defocused beam (10 μm) and low beam current (10 nA). This increases the efficiency of the measurement of mobile elements and minimizes the volatilisation of Na (Morgan & London, 1996). The following elements were measured in the glass; peak count times in brackets: Si (16 s), Ti (10 s), Al (10 s), Mg (20 s), Fe (20 s), P (10 s), K (16 s), Ni (10 s), Mn (20 s), Cr (16 s), Ca (10 s) and Na (16 s). Detection limits and primary standards used can be found

in the Supplementary Data. Acquired compositions were input into the Montierth *et al*. (1995) liquid-only thermometer calibrated specifically for Mauna Loa glasses with a +/- 10 °C uncertainty (internal and external error).

The matrix glass composition from the glassy selvage of M3 was used to calculate the minimum (closure) temperature for the diffusive timescale processes for the polyhedral olivines and a maximum temperature for the platy olivines. We measured 31 glass compositions where MgO contents range from 6.57-6.87 wt. % and give a temperature range of 1163-1169 °C. A temperature of 1167 °C (+/- 10 °C) was calculated from an average MgO of 6.7 wt. % (Table 1). An oxygen fugacity of NNO - 1 log units was applied, consistent with values used by other authors for this type of sample (Shea *et al*., 2015; Hartley *et al*., 2016; Rae *et al*., 2016).

Diffusion modelling

Diffusion timescales were modelled in AUTODIFF (Allan *et al*., 2013; Hartley *et al*., 2016; Pankhurst *et al*., 2018). We measured profiles from 48 olivine crystals across the platy and polyhedral populations, which we present in the results section. For input into the diffusion model, profiles of greyscale values were extracted perpendicular to the crystal edge from BSE images using *Image J* (Schneider *et al*., 2012). The stronger the contrast in backscatter, the stronger the contrast in composition between Fe and Mg; the precise values were calibrated using the major element compositions of the olivines analysed using EPMA. Best fit diffusion profiles to the calibrated BSE/EMPA

traverses were then modelled using AUTODIFF. A demo version of AUTODIFF can be found in the Supplementary Data. AUTODIFF is built around 1D composition-dependent diffusion curves calculated using a finite difference method. A profile with stronger contrast between core and rim will display increased asymmetry due to the compositional dependence of diffusivity, resulting in a different shape to the typical diffusion sigmoid. For a given set of initial boundary conditions e.g. temperature, oxygen fugacity, anisotropy and compositional contrast, all 1-D diffusion profiles are self-similar in time for any given composition dependence, i.e., diffusion after 4 time units will be twice as wide as at 1 time unit, but in all other aspects the curves are identical in their proportional curvature. For the measured diffusion profile if the boundary conditions (fixed) and the initial condition (assumed homogenous core) are known, the correct diffusion profile shape can be determined from these simulated diffusion curves as the one with the same degree of compositional contrast, and hence, the same asymmetry characteristics. Once that profile has been identified, it is fit to the data by applying a linear stretch along the distance axis. To fit measured profiles with the appropriately shaped 1D diffusion curve, the distance between the 20^{th} and 80^{th} percentile is calculated in the measured profile. The same range is measured in the pre-modelled curve, to give a stretch factor between the two. Curves are then overlaid, centred on the 50^{th} percentile of both curves as a reference point in the centre of the diffusion range (cf. Allan *et al.*, 2013; Hartley *et al.*, 2016). The profiles are fitted together at the mid-point of the distribution rather than at the crystal edge because this process needs a point that can

repeatedly be found on any profile. It is more difficult to repeatedly define the edge of the profile as it is often a free variable, and the edges of diffusion profiles are hard to identify against instrumental noise. The stretch factor is then applied to the pre-modelled curve to bring it into alignment with the natural data. In terms of determining a timescale, if for both sample and model

$$x \propto \sqrt{Dt} \qquad \text{(Eq. 1)}$$

and

$$x_{sample} = n x_{model} \qquad \text{(Eq. 2)}$$

where n denotes the stretch factor, then, by substitution and rearrangement

$$t_{sample} = \frac{n^2 D_{model} t_{model}}{D_{sample}} \qquad \text{(Eq.3)}$$

Equation 3 uses the stretch factor to relate the known model time of the pre-modelled curve with known diffusivity to the unknown diffusion time that elapsed within the sample, where D_{sample}, the Fe-Mg interdiffusivity of the sample, is constrained by sample-specific parameters of composition, oxygen fugacity, crystallographic orientation and temperature.

RESULTS

Lava lobe structure

Each lobe varies in crystal content, shape and vesicularity. Vesicularity is always higher in the upper crust than the lava core, as shown in Fig. 3(a). Vesicle cylinders

are evident throughout the lava core of the thicker lobes. These are vertical, 1-2 cm diameter, cylindrical features (~20 cm long) shown in Fig. 3(b). Segregated aphyric material containing up to 40 vol. % vesicles rests on the lava core where it is capped by gas-blisters (Fig. 3c). Mega vesicles are present at the top of the lava core in other lobes, as shown in Fig. 3(d). These internal lobe structures are common features of pāhoehoe lobes, thus underpinning the notion that the Moinui flow grew via processes of insulated lava transport and endogenous growth (e.g. Self et al., 1998; Thordarson & Self, 1998).

Lava lobe crystallinity and vesicularity

The abundances and relative proportions of vesicles and olivine crystals were calculated using *JMicrovision* point counting software on images of thin sections. Modal abundances described below are average values in the upper crust and lava core of samples M1-M4.

Initial field observations show that every part of the lobe contains both platy and polyhedral olivine crystals, although the absolute abundance and relative proportions may vary vertically and laterally within individual lobes (Fig. 2c). The glassy lobe selvages (i.e. the quenched outermost surface of the upper crust) best preserve the original crystal content of the lava at the time of emplacement (Guilbaud *et al.*, 2007). At Moinui the glassy selvages from lobe M3 contain 46% glass, 43% vesicles and 11% of olivine crystals (60 modal % polyhedral and 40 modal

% platy olivine). Across all samples, the upper crust (~10 cm) is composed of ~42% matrix, ~49% vesicles with ~9% olivine crystals (33 modal % polyhedral vs. 66 modal % platy olivine). The lava core is variable, composed of 47-64% matrix, 10-31 % vesicles and 19-32% olivine crystals (75-81 modal % polyhedral and 19-25 modal % platy olivine crystals). The total abundance of olivine crystals is highest in the lava core (19-32 modal %) and lowest (9 modal %) in the upper crust, and a little higher in the glassy selvage (11 modal %). Also, in the lava core the proportions of polyhedral olivine crystals are greater than that of the platy olivine crystals in three of the sampled lobes. Only in sample M4, which is from the lateral extremity of the flow field is the platy form more abundant. Conversely, the platy form is always more abundant in the upper crust and here, is always unzoned. In sample M4, the olivine crystals in the lava core are also more euhedral in shape than those in the lava core of lobes M1-M3. Examples of the polyhedral and platy olivine crystals present in all parts of the lava flow are shown in Fig. 4. The modal crystal abundances and proportion of vesicularity for each section of the lava lobes are further detailed in the Supplementary Data.

Mineralogy

Olivine textures and compositions

The polyhedral olivine crystals have a characteristic diameter of ~3 mm. In lobes M1-M3 they can be subhedral with round corners. This polyhedral olivine population is

almost exclusively comprised of glomerocrysts, with multiple crystals in contact along crystal faces. The zoning within the polyhedral olivines is normal (Fe-rich rim, Mg-rich core). Many of the polyhedral olivine crystals demonstrate broad diffusion widths and are compositionally zoned up to 300 μm into the crystals. Typically, where polyhedral olivines are present as part of a glomerocryst, the zoning follows the outer rim of the whole cluster, not the individual crystals. Despite the rounded exterior corners of the polyhedral olivines, the diffusion contours around the rims are continuous, suggesting diffusion occurred after the rounded morphology was established.

Platy olivine crystals vary in length from 1 to 3 mm and, in general, their orientation is random, implying that there is no flow fabric. The platy olivine crystals are commonly euhedral, with facets and sharp junctions of crystal faces, despite possessing irregular crystal edges. Figure 5 shows BSE images of the platy olivine with hollow segments within their interior. Where zoning is present in platy olivine crystals, it is normal (Fe-rich rim, Mg-rich core). Platy crystals with zonation typically only display that zoning in their outer margins with short diffusion widths (<50 μm). Such zoned platy olivines are only present within the core of the lava lobes. Platy olivines in the upper crusts of the lava lobes are unzoned. Both zoned and unzoned types have the same core compositions suggesting that they originated from the same population. Composition of unzoned platy olivine is given in the Supplementary Data.

The core and rim compositions of 48 olivine crystals (across both populations) exhibit a distinct bimodality as shown in Fig. 6 (a) and (b) – notably, a polyhedral crystal population with a core composition of Fo_{90-88} and a platy crystal population with a core composition of Fo_{83-82}. Polyhedral cores also exhibit high Ni (up to 0.51 wt. % NiO) compared to the platy cores (NiO up to 0.29 wt. %). The polyhedral and platy olivine crystals typically feature a core, inner zone and rim, illustrated in Fig. 6(c). Individual platy olivines have an inner zone ranging from Fo_{81} to Fo_{78} and a rim spanning Fo_{78} to $Fo_{64.}$ In contrast, the individual polyhedral olivines have an inner zone of Fo_{88-85} and a rim ranging from Fo_{84} to $Fo_{78.}$Thus, the core composition of the platy olivines (Fo_{83-82}) are consistent with the rim compositions of the polyhedral olivines. Core and rim values for both the polyhedral and platy olivines are shown in Table 2.

Whole-rock composition and olivine-liquid equilibrium

The high whole-rock MgO content (14-22 wt. %) of the Moinui lava and its high modal abundance of olivines define it as a picrite (Powers, 1955; Wilkinson & Hensel, 1988; Rhodes, 1995; Welsch *et al*., 2013), consistent with the composition of other Hawaiian picrites shown in Fig. 7. The picrites comprise only ~15% of the lava volume at Mauna Loa (Macdonald, 1949; Powers, 1955). The Moinui lava compositions are controlled by the addition of olivines (black arrow, Fig. 7), trending along a vector linking the MgO content of the polyhedral olivines and the

composition of the glass in the quenched lava selvages (Table 1). The whole-rock data can be found in the Supplementary Data.

The K_D(Fe-$Mg^{ol\text{-}liq}$) for olivines in equilibrium with their host melt is 0.30 +/- 0.03 (Roeder & Emslie, 1970). Matzen *et al*. (2011) conducted high temperature experiments (1302-1600°C) to calculate $K_{DFe\text{-}Mg}^{ol\text{-}liq}$for olivines in equilibrium with their high magnesian host melts. They report a high median K_D value of ~0.34. We assumed an Fe^{3+} value of ~10% in accordance with Rhodes & Vollinger (2005) for our K_D calculation. Using the equilibrium field of Roeder & Emslie (1970), Figure 8 shows that when compared to the glass composition of the lava selvages, the polyhedral olivine cores are not in chemical equilibrium with the melt ($K_{DFe\text{-}Mg}^{ol\text{-}liq}$ = 0.16-0.19)) and cluster to the left of the diagram. The platy olivine cores are in equilibrium with the melt and so therefore cluster in the middle of the diagram within the equilibrium zone ($K_{DFe\text{-}Mg}^{ol\text{-}liq}$ = 0.29-0.31)). Both the platy olivine and polyhedral olivine rims are out of equilibrium. These results do not change when considering the Matzen et al. (2011) equilibrium value.

Fe-Mg inter-diffusion modelling of timescales from the bladed and polyhedral olivine

Timescales were calculated for Fe-Mg inter-diffusion in zoned polyhedral and platy olivines. Basal crust samples were excluded from analysis due to oxidation of the olivine crystals. The diffusivity for Fe-Mg inter-diffusion in olivines is one of the

most robust and best-constrained of the known diffusivities in magmatic minerals (Dohmen & Chakraborty, 2007a and 2007b; Dohmen *et al.*, 2007; Brady & Cherniak, 2010; Chakraborty, 2010; Costa & Morgan, 2010). In basaltic systems, Fe-Mg inter-diffusion in olivine therefore is appropriate for the investigation of magmatic processes occurring over days to years (Dohmen & Chakraborty, 2007a and 2007b; Dohmen *et al.*, 2007).

We use a single temperature (1167 °C) for modelling all profiles from both polyhedral and platy olivine populations. The rims of the polyhedral olivines (mostly Fo_{84-83}) have a very similar composition to the bladed cores (Fo_{82}), suggesting growth from the same magma, albeit with earlier commencement of the crystallisation. The temperature of crystallisation and the diffusion time is difficult to establish without forcing commonality across the two populations. The zoned platy olivines have a variety of histories within the lava flow, where any particular temperature-time (T-t) history is more or less arbitrary. The modelling of these timescales relates to the cooling time of the lava tubes, which is variable with depth into the lava flow and sample. By modelling the platy olivines at a higher temperature (using melt in equilibrium with the platy cores rather than the rims), we ascertain a minimum time since the onset of diffusional re-equilibration. It is likely that the melt composition in equilibrium with the Fo_{83-82} platy cores, and the earlier melt composition that was in equilibrium with the Fo_{84-83} rims on the polyhedral olivines, would result in calculated temperatures within the uncertainty of the thermometer. As temperature

links to time, using a single temperature may of course have an impact on the diffusion timescales, however there are limits to how high the temperature could go without breaking the modelled equilibria.

In choosing an appropriate boundary condition for the modelling based on the shape and position on the diffusion profile, we applied an externally-buffered boundary condition to each of the diffusion profiles extracted from both populations of olivines, i.e., diffusive exchange occurred from the rim to the core of the crystal, with the rim in communication with the surrounding melt. This boundary condition can be described in the following equation assuming the initial rim composition as measured;

$$t = 0, C = C_0 \; for \; all \; x$$

$$t > 0, C = C_1, for \; all \; x > 0, \; and \; C_{(x,t)} = f(C,x,D,t), for \; all \; x > 0 \text{ (Eq. 4)}$$

Where C_0 is the initial composition, C_1 is the external buffer composition for t>0, D is diffusivity and x is distance. Whilst most of the measured polyhedral and platy olivines show a classic, monotonically varying diffusion curve (Fig. 9 a and b), consistent with an externally-buffered system, many polyhedral olivine grains display a strong kink towards the crystal rim as shown in Fig. 9 (c). This is accompanied by a rapid change in composition from ~Fo_{84} to Fo_{74} over a distance of 5-10 μm. If we model this (quench) growth as a diffusion-only process at appropriate temperatures, we get a maximum timescale of 7 days; a short growth period. Therefore, we take this thin rim to represent an overgrowth of a more evolved

composition driven by non-equilibrium crystal growth during magma ascent or transport at the surface. It most likely results from exposure to enhanced cooling rates in the very top of the conduit at the surface, where the cooling rates are at least 22-50 °C/hr, as calculated by Cashman *et al*. (1998) for a Kilauea active channel flow during a 1997 Kilauea eruption. Hence it is not representative of pre-eruptive timescales. In order to model only the true diffusion profile from core to the rim of a crystal, the composition of the outer rims of the polyhedral olivines were carefully separated from the quench rim according to the fit of the model to the profile at the rim. Rim compositions used for modelling range from Fo_{86-81}, but most rim compositions fall within the range of Fo_{84-83}.

Greyscale and EMPA profile shapes that were not consistent with diffusion-only modification were excluded from the dataset. In some cases (typically those with long diffusion widths) EMPA compositional profiles alone were input into the modelling.

A total of 83 profiles were measured in 48 olivine crystals from samples M1CL-M4CL and M1TC. Of these, 61 profiles (31 from bladed, 30 from polyhedral olivine) were suitable for modelling diffusion timescales, representing 41 olivine crystals from all of the sampled lobes (24 platy olivines and 17 polyhedral olivines). The remaining 22 profiles were rejected due to either: (i) analytical difficulties (n = 12), or (ii) the compositional gradient in the profiles was noticeably affected by

crystal growth and/or, apparent changes in boundary conditions (n = 10). Therefore, these profiles do not conform to the assumptions underpinning the modelling.

The largest sources of uncertainty in obtaining appropriate values for $D_{Fe\text{-}Mg}$ (Eq.5) and therefore for the error on the diffusion timescales are temperature (T), activation energy (ΔQ) and D_0 – the pre-exponential factor that relates crystal structure, jump frequency and distance. The terms were determined experimentally for Fe-Mg inter-diffusion in olivines by Dohmen & Chakraborty (2007a and 2007b). The effects of crystallographic orientation are also often incorporated (Buening & Buseck, 1973; Dohmen & Chakraborty, 2007a and 2007b; Dohmen *et al.*, 2007; Costa *et al.*, 2008; Brady & Cherniak, 2010; Chakraborty, 2010; Costa & Morgan, 2010).

$$D(Fe-Mg) = D_o \cdot exp\left(\frac{-Q - \Delta V\,(P - 10^5)}{R \cdot T}\right) \quad \text{(Eq. 5)}$$

It is critical that uncertainties are handled in a correct and consistent way to produce meaningful timescales. The upper and lower limits on the uncertainty were calculated by combining the ideal, maximum and minimum D values using each of the stated parameters (T, ΔQ, and D_0). The differences between (D_{ideal}) versus (D_{slow}) and (D_{ideal}) versus (D_{fast}) were calculated and the base 10 log ($\log_{10}$) was taken of the ideal, maximum and minimum D values.

Calculated Fe-Mg Timescales

Figure 10 (a) and (b) show further examples of traverses for modelling diffusion timescales from a platy and polyhedral olivine crystal. Figure 10 (c) shows the Fe-Mg diffusion timescales obtained from the polyhedral olivines and the platy olivines exhibit distinctly different distributions. The majority of the platy crystals define a tight cluster of timescales ranging from ~2-39 days, with 2 profiles giving somewhat longer timescales of 46 and 60 days. Timescales obtained from the polyhedral olivines span a much wider range, with timescales from ~52 days to over 3000 days (~9 years) and one profile that gives a timescale of 22 years. However, most of the obtained timescales fall within the range of 3 months to 6 years (n = 22). The average uncertainty on each calculated timescale is 0.34 log units (1σ). Timescales and uncertainties of measured profiles for a representative portion of the dataset are reported in Table 2.

DISCUSSION

Evolution of the bimodal olivine populations

Polyhedral olivine crystals

The distinct crystal shapes, bimodal compositions and diffusion timescales of the Moinui olivines are indicative of a range of processes occurring within the magma storage and transport system, pre-, syn- and post-eruption.

Equant, euhedral-subhedral crystals usually develop under equilibrium or near-equilibrium conditions at low degrees of undercooling and often slow growth

rates (Donaldson, 1976; Walker *et al.*, 1976; Lofgren, 1980; Deer *et al.*, 1997; Welsch et al., 2013). The slow growth and maturation of the primitive (Fo_{90-88}), high Ni (0.5 wt.% NiO; Sobolev *et al.*, 2005, 2007) polyhedral olivine cores are out of equilibrium with the melt, as shown in Fig. 8. Their position on the diagram indicates that the melt in which the polyhedral olivines are found does not have an MgO content that is sufficiently high to have produced the primitive olivine cores (Putirka, 2008). This suggests an origin within a more primitive melt, likely from a deeper source.

Whilst magma storage zones are not well constrained beneath Mauna Loa, using seismic P-wave tomography, Okubo et al. (1997) suggest high velocity regions may be present beneath the summit and rift zones at ~6-8 km depth. These are interpreted to be solidified ultramafic cumulates that represent upper crustal magma reservoirs and pathways. This depth range is consistent with Poland et al. (2014) who used InSAR data from 2002-2005 to indicate the presence of a dike-like structure opening at ~4-8 km depth. It is possible that this region could be the source of the polyhedral olivine cores, but they could also come from a deeper source. Experimental studies by Donaldson (1976) demonstrate that a cooling rate of only 0.5 °C/hr produces equant olivines while higher cooling rates i.e. 650 °C/hr, produce platy olivines. This supports the notion that the Moinui polyhedral olivines were formed and stored in a hot, primitive, slow-cooling (and hence deep) environment.

The Moinui magma has up to 32 modal % polyhedral olivines. The polyhedral olivines are often found as crystal clots with pore space between faces,

suggesting an origin from a mush zone (Nakagawa *et al*., 2002; Jerram *et al*., 2003). The melt that entrained the polyhedral olivines from deeper storage may have initially been under-saturated, whereby olivines will dissolve until saturation is reached giving rise to the observed rounded olivine grains. Although many of the polyhedral olivines show these rounded shapes, their diffused zones are not cross-cut by the crystal edges, implying that chemical dissolution had to occur prior to the onset of diffusion. This dissolution therefore likely occurred during transfer from a hot, deeper, primitive environment with low cooling rates (Donaldson, 1985) to shallower storage regions in the shallow crust (Passmore *et al*., 2012; Neave *et al*., 2013; Hartley *et al*., 2016). It is also possible that the rounding of these olivines could be an equilibrium textural response to minimising surface energy during growth (Holness *et al*., 2007; 2015), however this typically occurs within an intrusion or a pluton. What is key here is that the re-equilibration of these olivines post-dates the establishing of the rounded surface.

These primitive polyhedral cores (Fo_{90-88}) acquired more evolved rims (Fo_{86-78}) during ascent and within shallow storage and diffusively re-equilibrated due to decompression (Best, 2002) and chemical disequilibrium. As indicated by the normal zoning patterns and slow crystal growth rates, the polyhedral olivines must have resided for some time in the shallower storage environment. The subhedral nature of the polyhedral olivines may be further achieved due to annealing within cumulates at this level in the crust. Here, olivines were added incrementally over time,

explaining the diversity in core timescales and the olivine crystals interacted with the melt in a static environment (Passmore *et al.*, 2012). While conditions remained hot within these regions, the olivine crystals re-equilibrated through elemental diffusion. Localised convection of a liquid through the pore space of an otherwise static mush may also have driven diffusion (Hartley *et al.*, 2016) and diffusive relaxation continued over months to years while ambient conditions remained sufficient for diffusion to continue up until eruption.

Platy olivine crystals

The onset of nucleation and crystallisation of the platy olivines remains uncertain. Experiments by Lofgren *et al.* (1974) showed that significant crystallisation of a low Fe-Mg second mineral phase can lead to associated supersaturation of olivines in the liquid, which could give rise to the morphological change, i.e., the crystallisation of platy olivines at depth. However, the lack of evidence for a second mineral phase and the short diffusion timescales of the zoned platy olivines supports the notion that the platy olivines began to form at the time of eruption or when the magma was approaching the surface.

At higher cooling rates (>47 °C/hr) with significant undercooling (~20-60 - ΔT/°C) the habits of crystals forming in silicate melts become more skeletal or elongate (Donaldson, 1976; Walker *et al.*, 1976; Bianco & Taylor, 1977; Lofgren, 1980; Deer *et al.*, 1997; Faure *et al.*, 2003; Welsch *et al.*, 2013). Such high cooling rates and

degree of undercooling best explain the presence of platy olivines found in the Moinui lava. The hollows exhibited by the platy olivine crystals may indicate an origin as dendritic olivines, where incomplete maturation of initially hollow-plate shaped dendritic crystals has occurred. The irregular crystal edges found also show where the subsequent infilling has occurred, yet not been completed (Donaldson, 1976; Lofgren, 1980; Barnes. pers. comm.; Welsch et al. 2013).

We suggest that the platy crystal cores (Fo_{83-82}) nucleated a significant time after assimilation of the polyhedral cores and commencement of their diffusive re-equilibration, either just before the onset of eruption or perhaps during magma ascent. Degassing of the melt upon ascent and at the surface could have played a major role in rapidly undercooling the melt leading to supersaturation and re-equilibration of the melt to degassed conditions (Guilbaud *et al.*, 2007). The degassing likely induced rapid growth and the platy morphology. The absence of this dendritic growth on the edges of the polyhedral olivines may be due to a sudden nucleation of platy crystal core nucleation occurring on gas bubbles, therefore impeding observable dendritic overgrowth on the edges of the polyhedral olivines.

At the surface, further crystallisation and textural ripening occurred within the main magma pathway. The platy olivines in the crust were exposed to higher cooling rates than those residing in the lava core which may explain why the former are unzoned. These have grown *in situ* during lava flow emplacement, after lava is added to and becomes part of the crust and stops moving. The crystals grew and

were trapped when the crust solidified, preventing post-eruptive diffusion. This is supported by the apparent equilibrium between the host melt and the platy olivine cores (see Fig. 8), the lack of diffusion rims, overgrowths and flow alignment of the plates.

The zoned platy olivine crystals were resident in the insulated magma pathway (lava core) at magmatic temperatures where they are randomly distributed and continued to grow at a slower rate. They diffusively re-equilibrated as the melt composition changed through gradual cooling and degassing of residual volatiles (Crisp *et al.*, 1994; Guilbaud *et al.*, 2007). The more evolved compositions of the zoned and unzoned platy olivine rims infer late-stage crystallisation processes. Further evidence for this late crystallisation includes groundmass plagioclase crystals that are partly embedded into the edges of the platy olivines (Fig. 5c). Therefore, the short diffusion timescales of days or weeks recorded in the platy olivines represent lava residence time in the transport system (Fig. 10c). The fuller platy crystals that preserve longer timescales may have undergone a slower rate of crystallisation to form the crystal rim before the onset of diffusion. Alternatively, there may have been an early burst of crystallisation forming the core and then a later burst of crystallisation forming the more evolved rim of the platy olivines, before the onset of diffusion.

Within the lava flow

The polyhedral olivines have greater settling velocity because of their size and shape (Kerr & Lister, 1991) and therefore segregation of the two populations most likely took place during transport of the lava through the main lava pathway, where polyhedral olivines were removed from the melt column via settling. This is consistent with field observations demonstrating high concentration of polyhedral olivine in the lava core of individual lobes (Fig. 2 and 4b). Neither the platy nor the polyhedral olivine crystals have outermost rim zones that are in equilibrium with the melt. This is due to late-stage disequilibrium growth. The olivine may stay in a hot environment for as long as the tubes are active or until they have been picked up again by the moving lava and re-deposited elsewhere.

Linking crystal timescales and textures to magmatic process

The vents for the Moinui flow can be found at a few hundred meters of elevation below the summit (Kauahikaua, pers. comm), therefore the Moinui lava was likely sourced from within or very near the summit area. This is consistent with several studies that suggest (i) a magma storage zone is present at ~3-4 km depth beneath the summit crater and (ii) the presence of a dike-like structure that is present in the whole length of the summit crater (Rhodes, 1988; Poland *et al.*, 2014). Parfitt et al. (1995) showed that magma rise velocities of >0.024 m/s can lead to Strombolian-style eruptions, whereas velocities of <0.087 m/s can lead to Hawaiian-style eruptions. Given the lack of evidence regarding eruption style for the Moinui lava flow, we use

a proxy magma rise velocity of ~0.05 m/s (the transition between Strombolian and Hawaiian eruption styles) to calculate the time of magma ascent to the surface for the Moinui eruption. Applied to the Moinui eruption, from shallow storage at a depth of ~4 km, at this velocity, it would take ~20 hours for magma to reach the surface. After eruption, using an estimated velocity of 2 ms^{-1} for magma flowing through a tube (Hon *et al.*, 1994), it would take <5 hours for the Moinui magma to flow uninterrupted through the transport system to emerge at an active flow front at the coast 30 km away. The short timescales of hours for magma ascent and lava transport upon eruption, compared to the longer diffusion timescales calculated for both crystal populations, discounts simple magma migration as the *sole* control on diffusive processes within the olivine crystals. The long polyhedral olivine timescales support our hypothesis that magma stalled somewhere in the shallow storage system, and the polyhedral olivines it carries diffusively re-equilibrated. The polyhedral olivine timescales (Fig. 10c) are highly variable ranging from months to many years. This may reflect that the polyhedral cores are not accumulating within the shallow storage zone all at once. Magma may be passing through some form of mush conduit at depth over an extensive time period, with olivines (often as crystal clots) continuously assimilated. If the days-to-weeks timescales for platy olivine (interpreted to be related to transport at the surface) are subtracted from polyhedral olivine timescales, the timescales still range from months to years; this does not significantly affect these conclusions.

It has previously been inferred that magma typically rises into the shallow summit reservoir over several months to a year prior to eruption, as recorded by tilt meters and gas ratios (Tilling & Dvorak, 1993). Prior to at least two recent eruptions (July 1975 and March 1984), earthquakes have occurred at shallow and intermediate depths (0-5 km and 5-15 km, respectively), increasing in frequency, from 18 months before the onset of the eruption (Lockwood *et al.*, 1987; Decker *et al.*, 1995). Swarms of long period earthquakes have been recorded at depths of ~30 km beneath Mauna Loa and are interpreted to represent magma movement in the deep magma system through a focused crack of fixed geometry (Okubo & Wolfe, 2008). Whilst this movement occurs only weeks before eruption when it is associated with inflation at the surface, it is likely that most deep magma transfer takes place aseismically through a more diffuse network (Okubo & Wolfe, 2008). It is quite possible that some of the polyhedral olivines are recording these types of processes within their diffusion timescales.

The Moinui flow shares some similarities with other Mauna Loa flows, for example, the 1852 and 1868 picrites (Rhodes, 1995). They are all picritic flows with bimodal compositions of olivines (Fo_{89-83}) identified. However, within the 1852 and 1868 picrites, the majority of olivine falls within a narrower range of Fo_{89-87}, zoning is poorly developed and platy olivines are not found. The Moinui eruption is different from other "typical" Mauna Loa eruptions, because it contains no evidence of mixing between pockets of older, stored, shallow magma as inferred from the 1852 and 1868

picritic magmas (Rhodes, 1995) and other Mauna Loa lava flows (Gaffney, 2002). We have found no evidence of reverse zoning in either population of olivines which is commonly attributed to magm mixing processes. Primary melt compositions are unknown as no suitable melt inclusions were found within the polyhedral olivine cores. As there is also no evidence for melt-melt mixing in this suite, we suggest that the polyhedral olivines were added to the melt as a crystal slurry, with no, or an insignificant amount of associated melt.

Diffusion timescales, compositions and textures imply that the olivines beneath Mauna Loa spent months to years in shallow, pre-eruptive storage and that magma migration from depth to shallow storage happened incrementally over many years in preparation for the next eruption. This storage and transport model shares similarities with models both for Kīlauea (Tilling & Dvorak, 1993) and other similar volcanoes e.g. Piton de la Fournaise, La Réunion (Lénat *et al.*, 2012) and Krafla in Iceland (Ewart *et al.*, 1991).

We have demonstrated that interrogation of the crystal populations shows in detail: (i) the mulit-stage journey of the polyhedral olivines from depth to the surface; and (ii) nucleation and then crystallisation of the platy olivines, which took place after incorporation of the polyhedral olivines into the more-evolved magma. The primitive, high Ni polyhedral olivine cores of deeper origin were entrained in a melt that ascended and then stalled in a shallow storage system. The polyhedral cores grew a more Fe-rich inner rim over time in a static reservoir and diffusively re-

equilibrated over time. Polyhedral cores accumulated over a long period of time (years to decades) and the melt evolved to a lower MgO composition. The melt became saturated in volatiles and the platy cores nucleated. The system became over-pressurised and the melt started to ascend to the surface (Tait et al., 1989; Carricchi et al., 2018). During ascent, the polyhedral olivines acquired an outer quenched overgrowth rim. The melt degassed causing rapid undercooling of the melt, and this was accompanied by the growth of the platy cores into the platy morphology observed in the lava flow. Platy crystals caught in the upper lava flow crust remained unzoned, demonstrating relative uniformity of conditions to that point prior to quench. In the lava core, the platy olivines subsequently acquired more evolved rims and diffusively re-equilibrated; the polyhedral olivines also continued to diffusively re-equilibrate at their externals surface until the temperature lowered to a point where diffusive re-equilibration could no longer occurr. These processes are summarised in Fig. 11.

Potential analogue for komatiites

Komatiites are mostly of Archean age (greater than 2.5 Ga) and are believed to represent ultramafic liquids that erupted at high temperatures (between 1400°C and 1700°C), with viscosities of 0.1 to 1 Pa s and MgO contents of 18-35 wt %. They

demonstrate that the thermal conditions of the early Earth were significantly different to those of today (Huppert *et al.*, 1984).

Typically, komatiites exhibit layering whereby, post eruption, flows differentiate into an upper spinifex layer (upper A zone) and a lower cumulate layer composed of large closely packed equant crystals (lower B zone) (Pyke *et al.*, 1973; Arndt, 1986). Some flows have a relatively uniform olivine porphyritic texture, in which olivines concentrate in the centre *(*Arndt *et al.*, 1977). The Moinui flow does not show textural layering of the type seen in differentiated komatiite flows. Both the platy and polyhedral olivines are distributed throughout the flow, but are most concentrated in the centre, with polyhedral olivines occurring in higher modal abundances at the base of the lava core and concentrated near the base of the internal pathways. Two clear olivine populations are present: the platy olivines that may be analogous to the "random spinifex" that typifies the top of many komatiite lava lobes and polyhedral olivines analogous to the equant, "cumulate" olivines found in the core of komatiite lobes (Hill, 2001; Hill *et al.*, 2004). The platy/spinifex textured olivines possibly grew at the surface and *in situ* within the lava flow, the polyhedral cumulate olivines, may be, at least in part, carried crystals settling from the lava during flow. Although it has been suggested that most komatiites are erupted with very low phenocryst contents (Arndt *et al.*, 2008), we propose that the morphological and compositional features of the two populations within the Moinui are in

agreement with the proposals of Hill (2001) and Hill *et al.* (1995, 2004) relating to komatiite formation.

CONCLUSIONS

Field, petrological and geochemical investigations have revealed at least two crystal populations within the Moinui lava flow field erupted from the SWRZ of Mauna Loa, Hawai`i. These crystal populations are both chemically and texturally distinct and can be used to indicate storage, transport and emplacement processes of the Moinui lava flow field. The more primitive, equant crystal population is indicative of deeper magma transfer processes and shallow crustal storage pre-eruption over timescales of months to years, calculated using Fe-Mg diffusion modelling. These olivine crystals were deposited and re-distributed between lava tubes as activity switched between the main magma pathways. The more evolved, platy olivines nucleated and grew rapidly upon ascent and matured during emplacement of the flow field due to increased undercooling and supersaturation associated with degassing processes. Despite the Moinui being a well-insulated pāhoehoe flow, diffusion timescales can be interpreted and associated with storage, transport and emplacement mechanisms. The potential *in situ* crystallisation of the platy olivines versus the accumulation of the equant olivines may be used to infer a parallel, mixed origin for spinifex and cumulate olivine crystals found within komatiites.

ACKNOWLEDGMENTS

We thank the reviewers and the editor for their constructive comments and handling of the manuscript. We thank Richard Walshaw and Duncan Hedges for their assistance with the electron microprobe and the electron backscatter diffraction (EBSD) analyses and John-Wyn Williams for preparing the samples. We would like to thank Luke Wedmore and Frank Trusdell for assistance with the fieldwork.

FUNDING

This work was supported by the Natural Environment Research Council (NERC) as a PhD Studentship (NERC Grant Number 1367441).

REFERENCES

Allan, A. S. R., Morgan, D. J., Wilson, C. J. N. & Millet, M. A. (2013). From mush to eruption in centuries: Assembly of the super-sized Oruanui magma body. *Contributions to Mineralogy and Petrology* **166(1)**, 143–164.

Arndt, N. T. (1986). Differentiation of komatiite flows. *Journal of Petrology* **27(2)**, 279–301.

Arndt, N. T., Naldrett, A. J. & Pyke, D. R. (1977). Komatiitic and iron-rich tholeiitic lavas of munro township, Northeast Ontario. *Journal of Petrology* **18(2)**, 319–369.

Arndt, N. T., Lesher, M. C., Barnes, S. J. (2008). *Komatiite*. Cambridge University Press

Aubele, J. C., Crumpler, L. S. & Elston, W. E. (1988). Vesicle zonation and vertical structure of basalt flows. *Journal of Volcanology and Geothermal Research* **35(4)**, 349–374.

Barnard, W. M. (1995). Mauna Loa Volcano: Historical eruptions, exploration, and observations (1779–1910). *in Mauna Loa Revealed: Structure, Composition, History and Hazards. Geo* 1–19.

Best, M. G. (2002). *Igneous and Metamorphic Petrology Second Edition*. Blackwell Publishing.

Bianco, A. S. & Taylor, L. A. (1977). Applications of dynamic crystallization studies: Lunar olivine-normative basalts. *in Proceedings of the Lunar Science Conference 8th* 1593–1610.

Brady, J. B. & Cherniak, D. J. (2010). Diffusion in Minerals: An Overview of Published Experimental Diffusion Data. *Reviews in Mineralogy and Geochemistry* **72(1)**, 899–920.

Buening, D. K. & Buseck, P. R. (1973). Fe-Mg lattice diffusion in olivine. *Journal of Geophysical Research* **78(29)**, 6852–6862.

Carrichi, L., Sheldrake, T. E & Blundy, J. (2018). Modulation of magmatic processes by CO_2 flushing. *Earth and Planetary Science Letters*, **491,** 160-171

Cashman, K. V., Thornber, C. & Kauahikau, J. P. (1998). Cooling and crystallisation of lava in open channels, and the transition of Pahoehoe Lava to 'A'a. *Bulletin of Volcanology* **61**, 306-323

Chakraborty, S. (2010). Diffusion Coefficients in Olivine, Wadsleyite and

Ringwoodite. *Reviews in Mineralogy and Geochemistry* **72(1)**, 603–639.

Costa, C. & Morgan, D. (2010). Time Constraints from Chemical Equilibration in Magmatic Crystals. *Timescales of Magmatic Processes: From Core to Atmosphere*. Blackwell Publishing.

Costa, F. & Chakraborty, S. (2004). Decadal time gaps between mafic intrusion and silicic eruption obtained from chemical zoning patterns in olivine. *Earth and Planetary Science Letters* **227(3–4)**, 517–530.

Costa, F., Dohmen, R. & Chakraborty, S. (2008). Time Scales of Magmatic Processes from Modeling the Zoning Patterns of Crystals. *Reviews in Mineralogy and Geochemistry* **69(1)**, 545–594.

Crisp, J., Cashman, K. V, Bonini, J. A., Hougen, S. B. & Pieri, D. (1994). Crystallization history of the 1984 Mauna Loa lava flow. *Journal of Geophysical Research* **99**, 7177–7198.

Decker, R. W., Klein, F. W., Okamura, A. T. & Okubo, P. G. (1995). Forecasting eruptions of Mauna Loa volcano, Hawaii. American Geophysical Union conference abstract

Deer, W., Howie, R. & Zussman, J. (1997). *Rock forming minerals: Orthosilicates, Volume 1A*. The Geological Society.

Dohmen, R., Becker, H.-W. & Chakraborty, S. (2007). Fe–Mg diffusion in olivine I: experimental determination between 700 and 1,200°C as a function of composition, crystal orientation and oxygen fugacity. *Physics and Chemistry of Minerals* **34(6)**, 389–

407.

Dohmen, R. & Chakraborty, S. (2007a). Fe–Mg diffusion in olivine II: point defect chemistry, change of diffusion mechanisms and a model for calculation of diffusion coefficients in natural olivine. *Physics and Chemistry of Minerals* **34(6)**, 409–430.

Dohmen, R. & Chakraborty, S. (2007b). Erratum: Fe-Mg diffusion in olivine II: Fe–Mg diffusion in olivine II: point defect chemistry, change of diffusion mechanisms and a model for calculation of diffusion coefficients in natural olivine. *Physics and Chemistry of Minerals* **34**, 597-598.

Donaldson, C. H. (1976). An experimental investigation of olivine morphology. *Contributions to Mineralogy and Petrology* **57(2)**, 187–213.

Donaldson, C. H. (1985). The Rates of Dissolution of Olivine, Plagioclase, and Quartz in a Basalt Melt. *Mineralogical Magazine* **49(354)**, 683–693.

Ewart, J. A., Voight, B. & Björnsson, A. (1991). Elastic deformation models of Krafla Volcano, Iceland, for the decade 1975 through 1985. *Bulletin of Volcanology* **53(6)**, 436–459.

Faure, F., Trolliard, G., Nicollet, C., & Montel, J-M. (2003). A developmental model of olivine morphology as a function of the cooling rate and the degree of undercooling. *Contributions to Mineralogy and Petrology* **145,** 251-263

Gaffney, A. M. (2002). Environments of Crystallization and Compositional Diversity of Mauna Loa Xenoliths. *Journal of Petrology* **43(6)**, 963–981.

Garcia, M. O., Hulsebosch, T. P. & Rhodes, J. M. (1995). Olivine rich submarine basalts from the southwest rift zone of Mauna Loa Volcano: Implications for magmatic processes and geochemical evolution. *Mauna Loa Revealed: Structure, Composition, History, and Hazards. Geophysical Monograph 92*.

Guilbaud, M.-N., Blake, S., Thordarson, T. & Self, S. (2007). Role of Syn-eruptive Cooling and Degassing on Textures of Lavas from the AD 1783-1784 Laki Eruption, South Iceland. *Journal of Petrology* **48(7)**, 1265–1294.

Hartley, M. E., Morgan, D. J., Maclennan, J., Edmonds, M. & Thordarson, T. (2016). Tracking timescales of short-term precursors to large basaltic fissure eruptions through Fe–Mg diffusion in olivine. *Earth and Planetary Science Letters*. Elsevier B.V. **439**, 58–70.

Helz, R. T., Clague, D. A., Sisson, T. W. & Thornber, C. R. (2014). Petrologic Insights into Basaltic Volcanism at Historically Active Hawaiian Volcanoes Early History of Petrology at HVO. *Characteristics of Hawaiian Volcanoes: U.S. Geological Survey Professional Paper 1801*, 237–292.

Hill, R. E. T. (2001). Komatiite volcanology, volcanological setting and primary geochemical properties of komatiite-associated nickel deposits. *Geochemistry: Exploration, Environment, Analysis* **1(4)**, 365–381.

Hill, R. E. T., Barnes, S. J., Dowling, S. E. & Thordarson, T. (2004). Komatiites and nickel sulphide orebodies of the Black Swan area, Yilgarn Craton, Western Australia. 1. Petrology and volcanology of host rocks. *Mineralium Deposita* **39(7)**, 684–706.

Hill, R. E. T., Barnes, S. J., Gole, M. J. & Dowling, S. E. (1995). The volcanology of komatiites as deduced from field relationships in the Norseman-Wiluna greenstone belt, Western Australia. *Lithos* **34(1–3)**, 159–188.

Holness, M. B., Tegner, C.,. Nielsen, T. F. D., Stripp., G. & Morse, S. A. (2007). A textural record of solidification and cooling in the Skaergaard intrusion, East Greenland. *Journal of Petrology,* **48 (12)**, 2359-2377

Holness, M. B., Tegner, C., Namur, O. & Pilbeam., L. (2015). The earliest history of the Skaergaard magma chamber; a textural and geochemical study of the cambridge drill core. *Journal of Petrology*, **56 (6)**, 1199-1227

Hon, K., Kauahikaua, J., Denlinguer, R. & Mackay, K. (1994). Emplacement and inflation of pahoehoe sheet flows: Observations and measurements of active lava flows on Kilauea Volcano, Hawaii. *Geological Society of America Bulletin* **106(3)**, 351–370.

Huppert, H. E., Sparks, R. S. J., Turner, J. S. & Arndt, N. T. (1984). Emplacement and cooling of komatiite lavas. *Nature* **309(5963)**, 19–22.

Jarosewich, E., Nalen, J. A. & Norberg, J. A. (1980). Reference standards for electron microprobe analysis. *Geostandards Newsletter,* **4**, 43-47.

Jerram., D. A., Cheadle, M. J. & Philpotts, A. R. (2003). Quantifying the building blocks of igneous rocks: are clustered crystal frameworks the foundation? *Journal of Petrology* **44 (11)**, 2033-2051

Kerr, R. C. & Lister, J. R. (1991). The effects of shape on crytal settling and on the rheology of magmas. *The Journal of Geology*, **99 (3)**, 457-467

Lénat, J.-F., Bachèlery, P. & Merle, O. (2012). Anatomy of Piton de la Fournaise volcano (La Réunion, Indian Ocean). *Bulletin of Volcanology* **74(9)**, 1945–1961.

Lockwood, J. P., Dvorak, J. J., English, T. T., Koyanagi, R. Y., Okamura, A. T., Summers, M. L. & Tanigawa, W. R. (1987). Mauna Loa 1974-1984: A decade of intrusive and extrusive activity. *Volcanism in Hawaii* **Chapter 19**.

Lockwood, J. P. & Lipman, P. W. (1987). Holocene eruptive history of Mauna Loa volcano. *US Geological Survey Professional Paper Volcanism in Hawaii*.

Lofgren, G. (1980). Experimental studies on the dynamic crystallisation of silicate melts. *in Physics of Magmatic Processes*. Princeton University Press.

Lofgren, G., Donaldson, C. H., Williams, R. J., Mullins Jr., O. & Usselman, T. M. (1974). Experimentally reproduced textures and mineral chemistry of Apollo 15 quartz normative basalts. *in Proceedings of the Fifth Lunar Conference* 549–567.

Macdonald, G. A. (1949). Petrography of the island of Hawaii. *U.S. Geological Survey Professional Paper 214-D*, 51–96.

Marske, J. P., Pietruszka, A. J., Weis, D., Garcia, M. O. & Rhodes, J. M. (2007). Rapid passage of a small-scale mantle heterogeneity through the melting regions of Kilauea and Mauna Loa volcanoes. *Earth and Planetary Science Letters* **259**, 34-50

Matzen, A. K., Baker, M. B., Beckett, J. R. & Stopler, E. M. (2011). Fe-Mg partitioning

between olivine and high-magnesian melts and the nature of hawaiian parental liquids. *Journal of Petrology,* **52**, **(7&8)**, 1243-1263

Montierth, C., Johnston, A. D. & Cashman, K. V. (1995). An empirical glass-composition-based geothermometer for Mauna Loa Lavas. *in Mauna Loa Revealed: Structure, Composition, History and Hazards. Geophysical Monograph 92* 207–217.

Morgan, G. B. V. & London, D. (1996). Optimizing the electron microprobe analysis of hydrous alkali aluminosilicate glasses. *American Mineralogist* **81**, 1176–1185.

Nakagawa, M., Wada, K. & Wood, P. (2002). Mixed magmas, mush chambers and eruption triggers: evidence from zoned clinopyroxene phenocrysts in andesitic scoria from the 1995 eruptions of Ruapehu volcano, New Zealand. *Journal of Petrology* **43 (11),** 2279-30

Nakamura, A. & Schmalzried, H. (1983). On the nonstoichiometry and point defects of olivine. *Physics and Chemistry of Minerals* **10(1)**, 27–37.

Neave, D. A., Passmore, E., Maclennan, J., Fitton, G. & Thordarson, T. (2013). Crystal-Melt Relationships and the Record of Deep Mixing and Crystallization in the AD 1783 Laki Eruption, Iceland. *Journal of Petrology* **54(8)**, 1661–1690.

Okubo, P. G., Benz, H. M. & Chouet, B. A. (1997) Imaging crustal magma sources beneath Mauna Loa and Kilauea volcanoes, Hawaii. *Geology* **25(10)**, 867-870

Okubo, P. G. & Wolfe, C. J. (2008). Swarms of similar long-period earthquakes in the mantle beneath Mauna Loa Volcano. *Journal of Volcanology and Geothermal Research*.

Elsevier B.V. **178(4)**, 787–794.

Pankhurst, M. J., Morgan, D. J., Thordarson, T. & Loughlin, S. C. (2018). Magmatic crystal records in time, space, and process, causatively linked with volcanic unrest. *Earth and Planetary Science Letters*. Elsevier B.V. **493**, 231–241.

Parfitt, E. A., Wilson, L. & Neal, C. A. (1995). Factors influencing the height of Hawaiian lava fountains: implications for the use of fountain height as an indicator of magma gas content. *Bulletin of Volcanology.* **57,** 440-450

Passmore, E., Maclennan, J., Fitton, G. & Thordarson, T. (2012). Mush Disaggregation in Basaltic Magma Chambers: Evidence from the AD 1783 Laki Eruption. *Journal of Petrology* **53(12)**, 2593–2623.

Perring, C. S., Barnes, S. J., Verrall, M. & Hill, R. E. T. (2004). Using automated digital image analysis to provide quantitative petrographic data on olivine–phyric basalts. *Computers & Geosciences* **30(2)**, 183–195.

Pietruszka, A. J., Norman, M. D., Garcia, M. O., Marske, J. P. & Burns, D. H. (2013) Chemical heterogeneity in the Hawaiian mantle plume from the alteration and dehydration of recycled oceanic crust. *Earth and Planetary Science Letters* **361,** 298-309

Poland, M. P., Miklius, A. & Montgomery-Brown, E. K. (2014). Magma Supply, Storage, and Transport at Shield-Stage Hawaiian Volcanoes. *U.S. Geological Survey Professional Paper 1801* **2010**, 1–52.

Powers, H. A. (1955). Composition and origin of basaltic magma of the Hawaiian

Islands. *Geochimica et Cosmochimica Acta* **7**, 77–107.

Putirka, K. (2008), Thermometers and barometers for volcanic systems. *Reviews in Mineralogy & Geochemistry*, **69**, 61-120

Pyke, D. R., Naldrett, A. J. & Eckstrand, O. R. (1973). Archean ultramafic flows in Munro Township, Ontario. *Bulletin of the Geological Society of America* **84(3)**, 955–978.

Rae, A. S. P., Edmonds, M., Maclennan, J., Morgan, D., Houghton, B., Hartley, M. E. & Sides, I. (2016). Time scales of magma transport and mixing at Kīlauea Volcano, Hawai'i. *Geology* **44(6)**, 463–466.

Rhodes, J. M. (1988). Geochemistry of the 1984 Mauna Loa Eruption: Implications for magma storage and supply. *Journal of Geophysical Research* **93(B5)**, 4453.

Rhodes, J. M. (1995). The 1852 and 1868 Mauna Loa picrite eruptions: Clues to parental magma compositions and the magmatic plumbing system. *in Mauna Loa Revealed: Structure, Composition, History and Hazards. Geophysical Monograph 92,* 241–262.

Rhodes, J. M. & Hart, S. R. (1995). Episodic trace element and isotopic variations in historical mauna loa lavas: Implications for magma and plume dynamics. *Geophysical Monograph Series* **92**, 263–288.

Rhodes, J. M. & Vollinger, M. J. (2005). Ferric/ferrous ratios in 1984 Mauna Loa lavas: a contribution to understanding the oxidation state of Hawaiian magmas. *Contributions to Mineralogy and Petrology*, **29(4)**, 666-674

Rhodes, J. M., Wenz, K. P., Neal, C. A., Sparks, J. W. & Lockwood, J. P. (1989). Geochemical evidence for invasion of Kilauea's plumbing system by Mauna Loa magma. *Nature* 257–260.

Roeder, P. L. & Emslie, R. F. (1970). Olivine-Liquid Equilibrium. *Contributions to Mineralogy and Petrology* **29**, 275–289.

Schneider, C. A., Rasband, W. S. & Eliceiri, K. W. (2012). NIH Image to ImageJ: 25 years of image analysis. *Nature Methods* **9(7)**, 671–675.

Self, S., Keszthelyi, L. & Thordarson, T. (1998). the Importance of Pahoehoe. *Annual Review of Earth Planetary Sciences* **26**, 81–110.

Shea, T., Lynn, K. J. & Garcia, M. O. (2015). Cracking the olivine zoning code: Distinguishing between crystal growth and diffusion. *Geology* **43(10)**, 935-938.

Sobolev, A. V., Hofmann, A. W., Sobolev, S. V. & Nikogosian, I. K. (2005). An olivine free mantle source of Hawaiian shield basalts. *Nature* **43,** 590-597

Sobolev. A. V., Hofmann, A. W. & Kuzmin, D. V. (2007). The amount of recycled crust in sources of mantle-derived melts. *Science* **316,** 412-417

Tait, S., Jaupart, C., & Vergniolle, S. (1989). Pressure, gas content and eruption periodicity of a shallow, crystallising magma chamber. *Earth and Planetary Science Letters*, **92**, 107-123

Thordarson, T. & Self, S. (1998). The Roza Member, Columbia River Basalt Group: A gigantic pahoehoe lava flow field formed by endogenous processes? *Journal of*

Geophysical Research: Solid Earth **103**, 27411–27445.

Tilling, R. I. & Dvorak, J. J. (1993). Anatomy of a basaltic volcano. *Nature* 125–133.

Trusdell, F. A. & Lockwood, J. P. (2017). *Geologic Map of the Northeast Flank of Mauna Loa Volcano, Island of Hawai'i, Hawaii*. *USGS Scientific Investigations Map 2932-A*.

Walker, D., Kirkpatrick, R. J., Longhi, J. & Hays, J. F. (1976). Crystallization history of lunar picritic basalt sample 12002: Phase-equilibria and cooling-rate studies. *Bulletin of the Geological Society of America* **87(5)**, 646–656.

Walker, G. P. L. (1991). Structure, and origin by injection of lava under surface crust, of tumuli, 'lava rises', 'lava-rise pits', and 'lava-inflation clefts' in Hawaii. *Bulletin of Volcanology* **53(4)**, 546–558.

Welsch, B., Faure, F., Famin, V., Baronnet, A. & Bachelery, P. (2013). Dendritic crystallisation: A single process for all the textures of olivine in basalts? *Journal of Petrology* **54 (3)**, 539-574

Wilkinson, J. F. G. & Hensel, H. D. (1988). The petrology of some picrites from Mauna Loa and Kilauea volcanoes, Hawaii. *Contributions to Mineralogy and Petrology* 326–345.

FIGURE CAPTIONS

Figure 1: A map of the western part of the Big Island of Hawai`i, showing the location of the Moinui lava flow field (orange) on the west flank of Mauna Loa. The

digital elevation model is from the Shuttle Radar Topography Mission (SRTM) at 30 m resolution. The black triangle indicates the summit caldera of Mauna Loa, Moku`āweoweo, at 4167 m above sea level. The northeast (NERZ) and southwest rift zone (SWRZ) of Mauna Loa are also indicated. The yellow star on the inset map highlights the position of Big Island in the Hawaiian archipelago. The magenta star highlights the location of outcrops where the lava flow was sampled.

Figure 2: (a) Field photograph and sketch overlay of Outcrop 1 (OC1) showing a stack of inflated lobes and the location of samples M1 and M3 (yellow dots). The elongate tumulus represents a section of the lava transport system (i.e. an internal pathway). The red circle highlights an inflation cleft – see text for more details. (b) Field photograph and sketch overlay of Outcrop 2 (OC2) showing the distribution of lobes on a smaller scale and the location of sample M2 (yellow dot). The black lines indicate lobe outlines and individual lobes are labelled in red with an "L" followed by a number, as referred to in the main text. Examples of upper crust, lava core and basal crust are indicated by the green labels. (c) Example field logs through the Moinui lava flow illustrating vertical arrangements of vesicles and olivine crystals within in a typical Moinui lobe. Note: outcrop 3 and sample M4 are not included here, but the site is in the same roadcut ~30 m down the road and close to the edge of the flow field.

Figure 3: Field photographs of vesicular lava and segregation structures within Moinui lava lobes: (a) vesicular upper crust (middle part); (b) vesicle cylinders (VCs) in the lava core containing vesicular segregated material; (c) crystal poor, vesicular segregated material at the base of a gas blister. This is also visible on Fig. 2a to the left of the photograph; (d) a train of megavesicles along an indistinct (partly obliterated) horizontal vesicle sheet (HVS).

Figure 4: (a, c and e): Platy olivine examples highlighted by green circles within the Moinui lava as seen in the field (a); under an optical microscope (c) and in backscattered electron images (e). (b, d and f): Polyhedral olivines in the Moinui lava core, as seen in the field (b); under an optical microscope (d) and in a backscattered electron image (f).

Figure 5: (a) and (b) Platy olivine featuring a series of hollows along the length of the crystal axis suggesting origin from initial dendritic morphology; (c) shows irregular, non-planar crystal edges along a platy olivine where subsequent infilling and growth occurred.

Figure 6: (a) Core compositions of the Moinui olivine populations. The bimodal split of the core compositions corresponds to the bimodality of the olivine shapes – polyhedral *versus* platy. (b) Rim compositions of the Moinui olivine populations. The

bimodal split of the rim compositions corresponds to the bimodality of the olivine shapes – polyhedral versus platy (c) Annotated SEM images indicating the compositional zones of the polyhedral and platy olivines.

Figure 7: Whole-rock SiO_2 plotted against (a) MgO and (b) Al_2O_3. Light grey points are published data for Hawaiian picrites selected from the GEOROC database (http://georoc.mpch-mainz.gwdg.de/georoc/). These data can be found in the Supplementary Data. Blue points are data from the basal crust, lava core and upper crust of Moinui lobe M1. The black triangle represents the projected Fo_{89}-olivine of the Moinui magma. The black arrow represents the addition of olivine.

Figure 8: Rhodes diagram adapted from Putirka, (2008). The Mg# of the Moinui olivine *vs* the Mg# of the glassy selvage are plotted for cores and rims of both olivine populations. The platy olivine cores cluster within a range considered to be in equilibrium with the host melt, whereas the polyhedral olivine cores cluster are out of equilibrium, clustering to the left of the diagram suggesting that olivine removal was the controlling process for disequilibrium with the host melt, suggesting that the host melt was too poor in Mg to crystallise these compositions. Both the platy olivine and the polyhedral rims are out of equilibrium, showing vertical distributions indicating late-stage disequilibrium growth. Polyhedral rims $<Fo_{80}$ are from the outer

quenched rim. Platy rims less than <Fo_{70} (8 rim compositions) are not shown as they are so far out of equilibrium.

Figure 9: Examples of the diffusion profile shapes found within the Moinui dataset: (a) Shorter platy olivine profile (M1C_2A); (b) Longer, polyhedral olivine profile (M1C_A2); (c) The longer, polyhedral olivine profile often has a rapidly quenched growth rim towards the very edge of the crystal (M3C_D1). This quench was not modelled as it is not thought to be diffusion related, but rather due to quench growth during ascent to/at the surface.

Figure 10: Compositional profiles from the rim to the homogeneous plateau of platy and polyhedral olivine populations and the obtained timescales. Calibrated compositions (blue diamonds) along a profile through: (a) a platy olivine (M1C_10A), profile indicated by the blue line on the backscattered electron image; (b) a polyhedral olivine (M4C_C2), profile indicated by the yellow line on the backscattered electron image. In each case the red line is the best fit diffusion model. The position of the profile extends into negative values simply due to the fitting methods used as discussed in the text. In (a) the diffusion model gives a timescale of 36 days. In (b) the quenched rim is represented by values below ~Fo_{84}, as indicated by the blue arrow. This profile is a lot broader than that retrieved from the platy olivine. The diffusion model gives a best fit timescale of 503 days; (c) Distribution of timescales obtained from all profiles. The timescales calculated from platy olivine

(white bars) are constrained to days to weeks, whereas the timescales calculated from the polyhedral olivine (black bars) span a range from weeks to years (see text for more details).

Figure 11: Schematic summary of the crustal to surface processes that operated at Mauna Loa, prior to and during the Moinui eruption. The primitive, high Ni polyhedral olivines cores of deeper origin were incorporated, often as glomerocrysts, into a melt that ascended and became stalled in a shallow storage zone. Here, they acquired more evolved inner rims in static reservoir and diffusively re-equilibrated over time. This process occurred repeatedly over a period of time from months to years before eruption, continuously assimilating polyhedral olivine, and the melt evolved to a lower MgO composition. The melt became saturated in volatiles, and over-pressurisation of the shallow chamber lead to the onset of eruption. The platy cores nucleated and the melt degassed during ascent and upon emplacement at the surface. This degassing rapidly undercooled the melt, and the platy cores grew into the platy morphology. Those in the crust grew *in situ* and remain unzoned, whereas those in the lava core remained hot, acquired a rim of more evolved composition and diffused until the flow sufficiently cooled. During ascent, the polyhedral olivines acquired quenched rim overgrowths and upon eruption the polyhedral olivines continued to diffuse in the lava transport system until the lava flow sufficiently cooled.

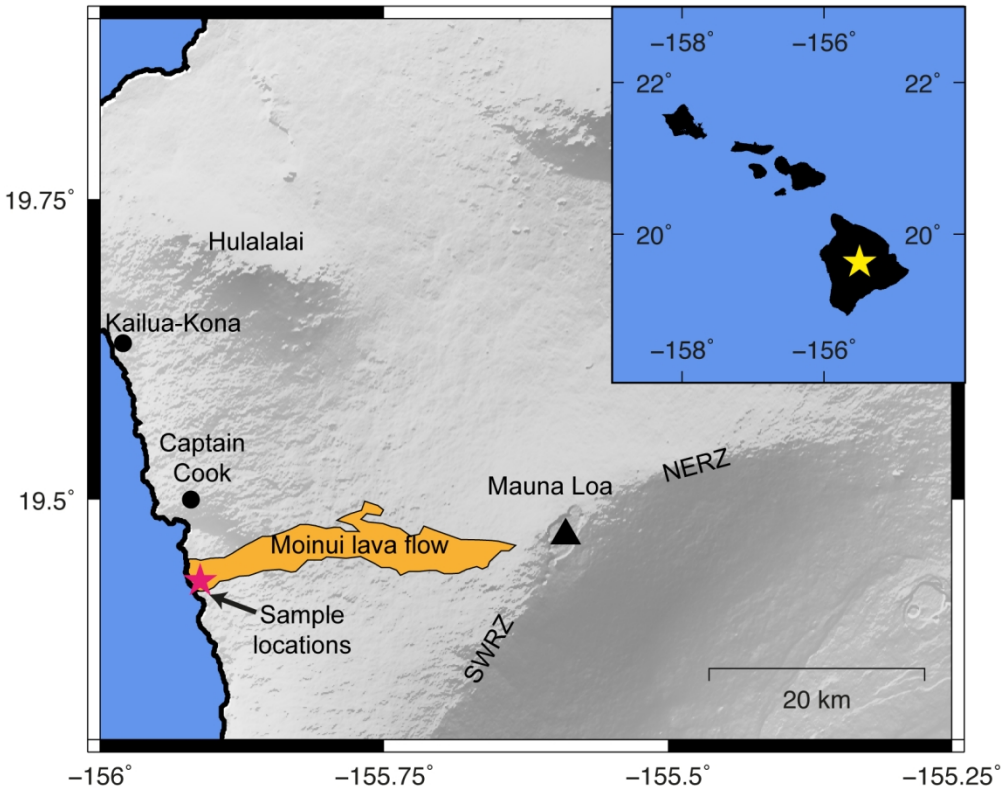

Figure 1: A map of the western part of the Big Island of Hawai`i, showing the location of the Moinui lava flow field (orange) on the west flank of Mauna Loa. The digital elevation model is from the Shuttle Radar Topography Mission (SRTM) at 30 m resolution. The black triangle indicates the summit caldera of Mauna Loa, Moku`āweoweo, at 4167 m above sea level. The northeast (NERZ) and southwest rift zone (SWRZ) of Mauna Loa are also indicated. The yellow star on the inset map highlights the position of Big Island in the Hawaiian archipelago. The magenta star highlights the location of outcrops where the lava flow was sampled.

140x111mm (300 x 300 DPI)

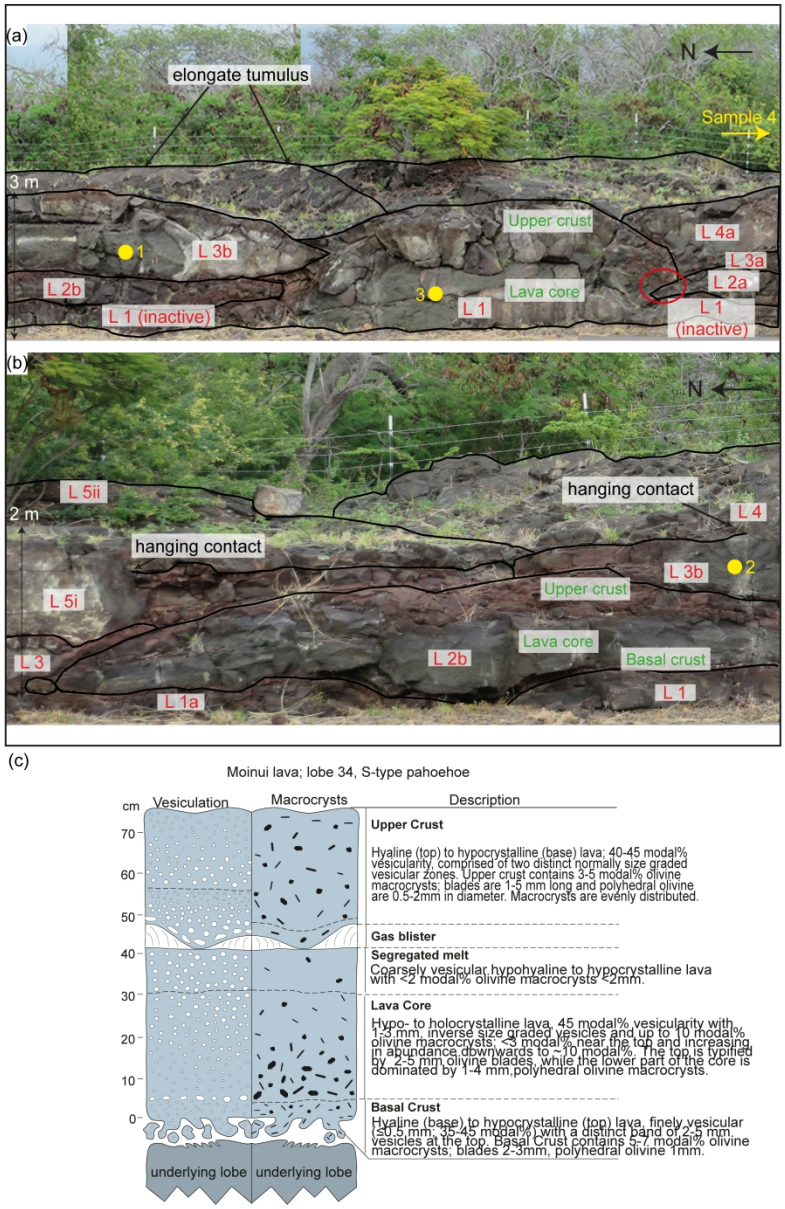

Figure 2: (a) Field photograph and sketch overlay of Outcrop 1 (OC1) showing a stack of inflated lobes and the location of samples M1 and M3 (yellow dots). The elongate tumulus represents a section of the lava transport system (i.e. an internal pathway). The red circle highlights an inflation cleft – see text for more details. (b) Field photograph and sketch overlay of Outcrop 2 (OC2) showing the distribution of lobes on a smaller scale and the location of sample M2 (yellow dot). The black lines indicate lobe outlines and individual lobes are labelled in red with an "L" followed by a number, as referred to in the main text. Examples of upper crust, lava core and basal crust are indicated by the green labels. (c) Example field logs through the Moinui lava flow illustrating vertical arrangements of vesicles and olivine crystals within in a typical Moinui lobe. Note: outcrop 3 and sample M4 are not included here, but the site is in the same roadcut ~30 m down the road and close to the edge of the flow field.

310x472mm (300 x 300 DPI)

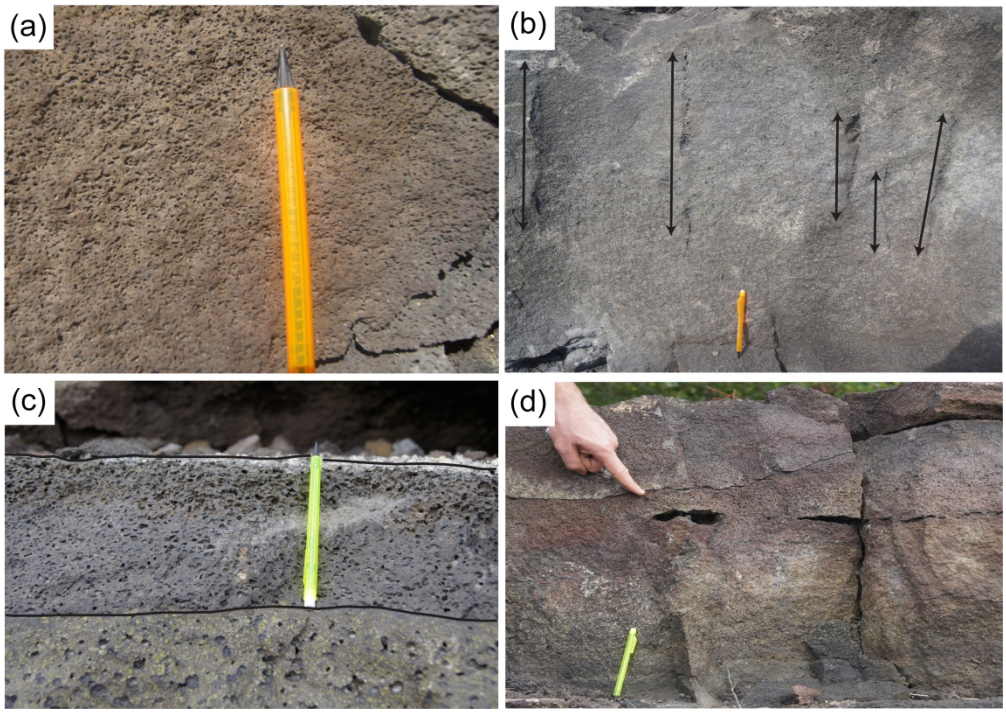

Figure 3: Field photographs of vesicular lava and segregation structures within Moinui lava lobes: (a) vesicular upper crust (middle part); (b) vesicle cylinders (VCs) in the lava core containing vesicular segregated material; (c) crystal poor, vesicular segregated material at the base of a gas blister. This is also visible on Fig. 2a to the left of the photograph; (d) a train of megavesicles along an indistinct (partly obliterated) horizontal vesicle sheet (HVS).

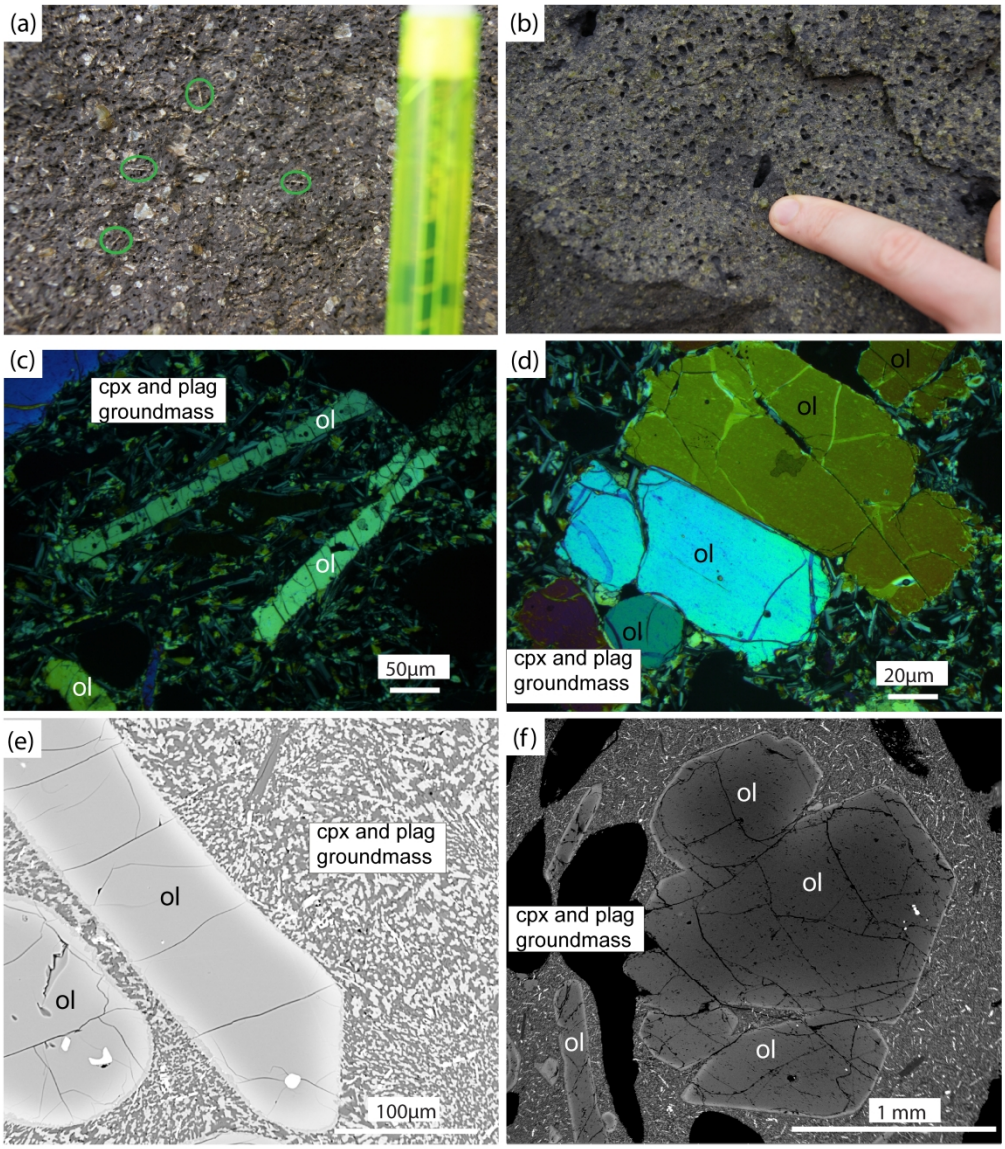

Figure 4: (a, c and e): Platy olivine examples highlighted by green circles within the Moinui lava as seen in the field (a); under an optical microscope (c) and in backscattered electron images (e). (b, d and f): Polyhedral olivines in the Moinui lava core, as seen in the field (b); under an optical microscope (d) and in a backscattered electron image (f).

673x774mm (150 x 150 DPI)

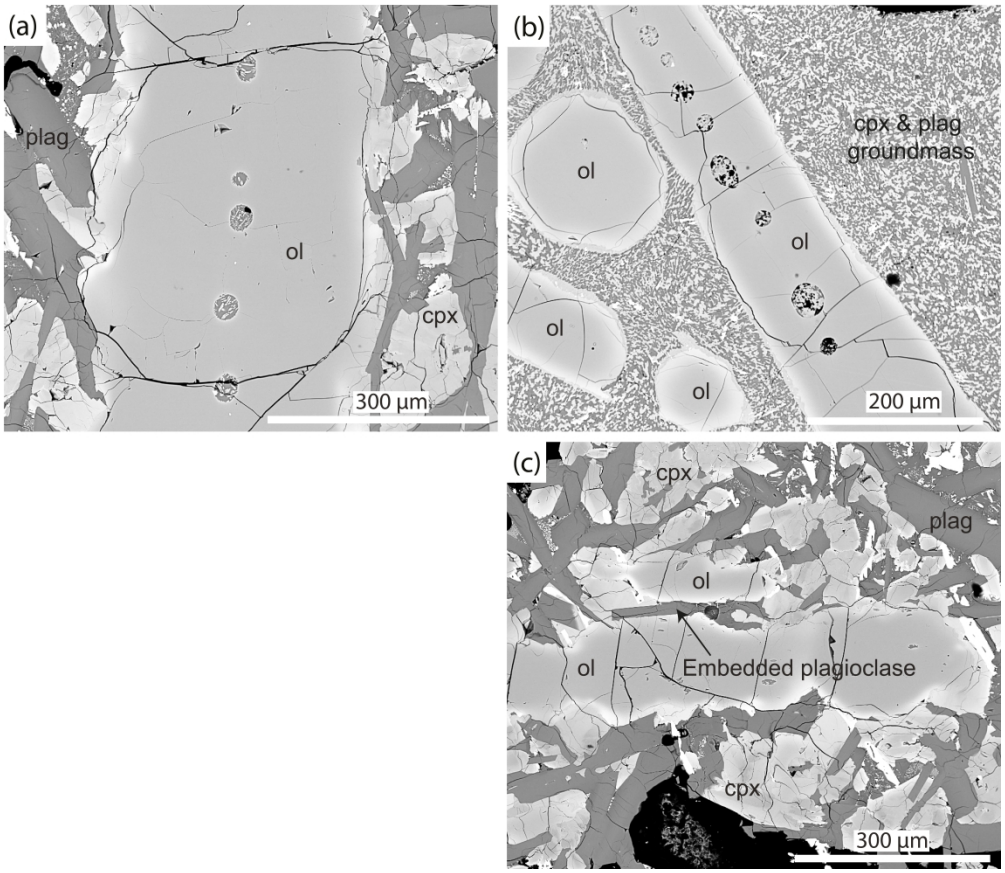

Figure 5: (a) and (b) Platy olivine featuring a series of hollows along the length of the crystal axis suggesting origin from initial dendritic morphology; (c) shows irregular, non-planar crystal edges along a platy olivine where subsequent infilling and growth occurred.

474x409mm (600 x 600 DPI)

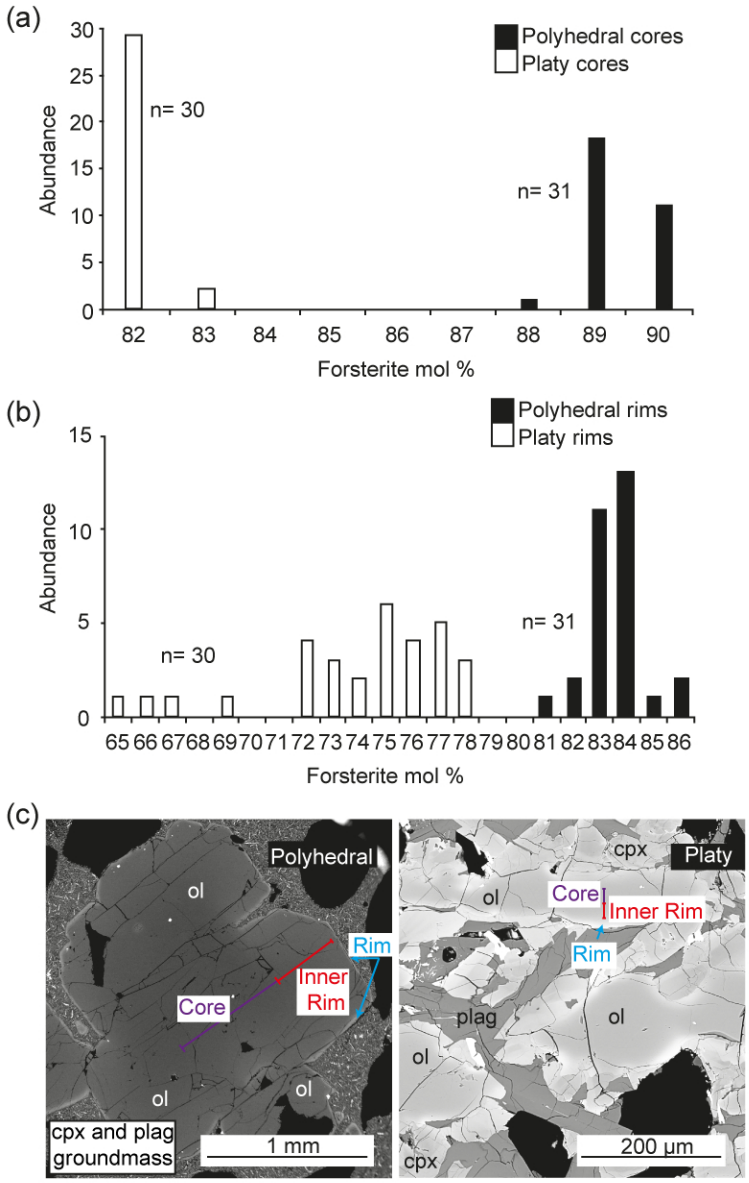

Figure 6: (a) Core compositions of the Moinui olivine populations. The bimodal split of the core compositions corresponds to the bimodality of the olivine shapes – polyhedral versus platy. (b) Rim compositions of the Moinui olivine populations. The bimodal split of the rim compositions corresponds to the bimodality of the olivine shapes – polyhedral versus platy (c) Annotated SEM images indicating the compositional zones of the polyhedral and platy olivines.

147x211mm (150 x 150 DPI)

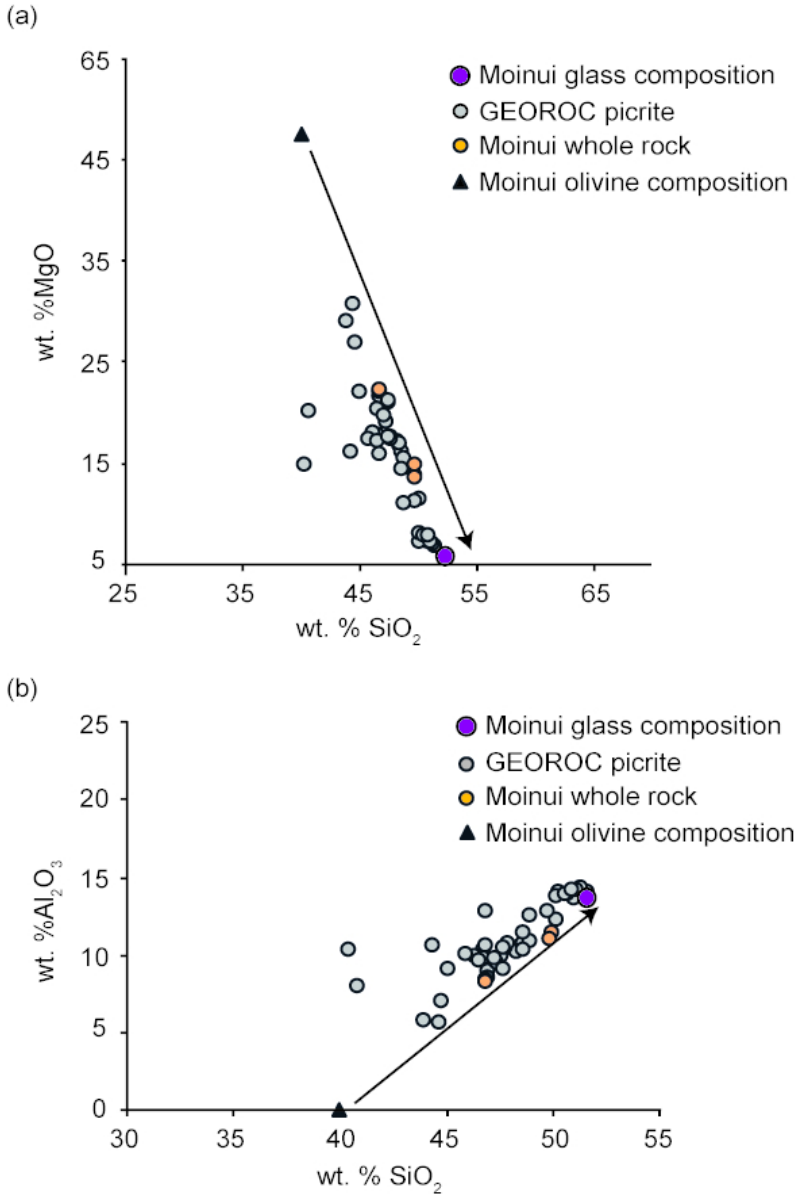

Figure 7: Whole-rock SiO2 plotted against (a) MgO and (b) Al2O3. Light grey points are published data for Hawaiian picrites selected from the GEOROC database (http://georoc.mpch-mainz.gwdg.de/georoc/). These data can be found in the Supplementary Data. Blue points are data from the basal crust, lava core and upper crust of Moinui lobe M1. The black triangle represents the projected Fo89-olivine of the Moinui magma. The black arrow represents the addition of olivine.

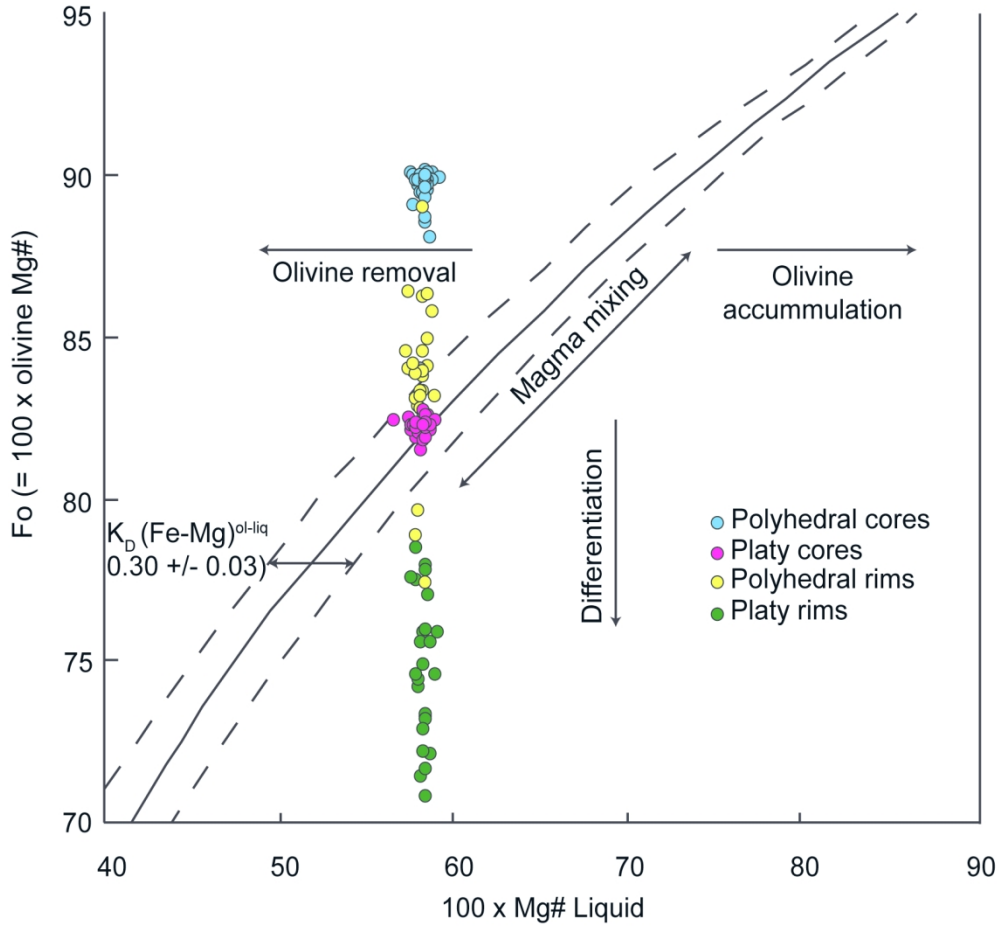

Figure 8: Rhodes diagram adapted from Putirka (2008). The Mg# of the Moinui olivine vs the Mg# of the glassy selvage are plotted for cores and rims of both olivine populations. The platy olivine cores cluster within a range considered to be in equilibrium with the host melt, whereas the polyhedral olivine cores cluster are out of equilibrium, clustering to the left of the diagram suggesting that olivine removal was the controlling process for disequilibrium with the host melt, suggesting that the host melt was too poor in Mg to crystallise these compositions. Both the platy olivine and the polyhedral rims are out of equilibrium, showing vertical distributions indicating late-stage disequilibrium growth. Polyhedral rims < Fo80 are from the outer quenched rim. Platy rims less than < Fo70 (8 rim compositions) are not shown as they are so far out of equilibrium.

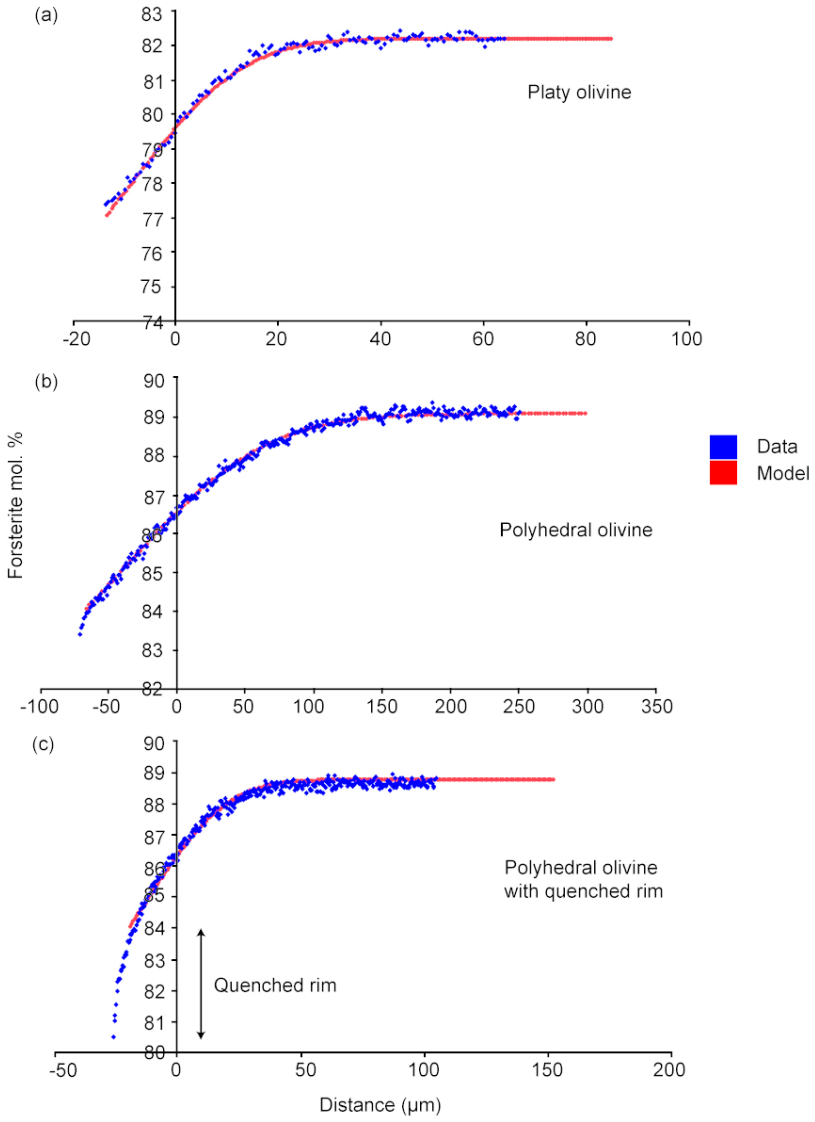

Figure 9: Examples of the diffusion profile shapes found within the Moinui dataset: (a) Shorter platy olivine profile (M1C_2A); (b) Longer, polyhedral olivine profile (M1C_A2); (c) The longer, polyhedral olivine profile often has a rapidly quenched growth rim towards the very edge of the crystal (M3C_D1). This quench was not modelled as it is not thought to be diffusion related, but rather due to quench growth during ascent to/at the surface.

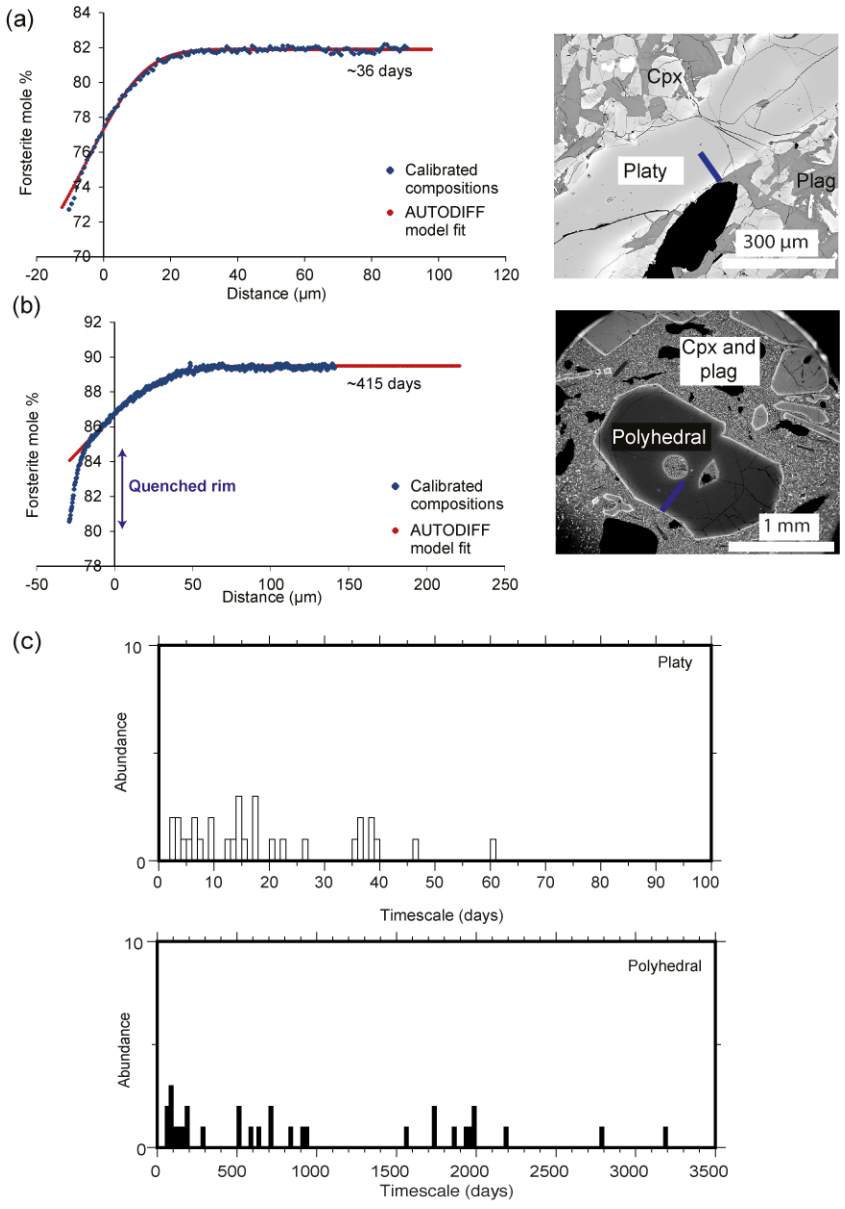

Figure 10: Compositional profiles from the rim to the homogeneous plateau of platy and polyhedral olivine populations and the obtained timescales. Calibrated compositions (blue diamonds) along a profile through: (a) a platy olivine (M1C_10A), profile indicated by the blue line on the backscattered electron image; (b) a polyhedral olivine (M4C_C2), profile indicated by the yellow line on the backscattered electron image. In each case the red line is the best fit diffusion model. The position of the profile extends into negative values simply due to the fitting methods used as discussed in the text. In (a) the diffusion model gives a timescale of 36 days. In (b) the quenched rim is represented by values below ~Fo84, as indicated by the blue arrow. This profile is a lot broader than that retrieved from the platy olivine. The diffusion model gives a best fit timescale of 503 days; (c) Distribution of timescales obtained from all profiles. The timescales calculated from platy olivine (white bars) are constrained to days to weeks, whereas the timescales calculated from the polyhedral olivine (black bars) span a range from weeks to years (see text for more details).

147x211mm (150 x 150 DPI)

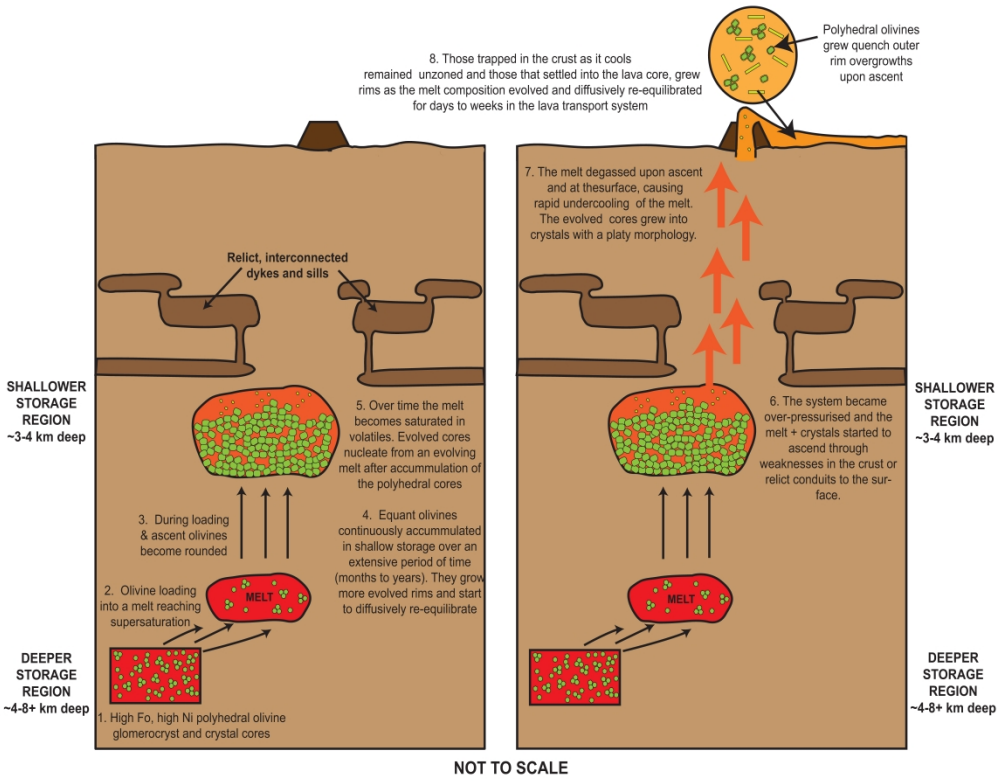

Figure 11: Schematic summary of the crustal to surface processes that operated at Mauna Loa, prior to and during the Moinui eruption. The primitive, high Ni polyhedral olivines cores of deeper origin were incorporated, often as glomerocrysts, into a melt that ascended and became stalled in a shallow storage zone. Here, they acquired more evolved inner rims in static reservoir and diffusively re-equilibrated over time. This process occurred repeatedly over a period of time from months to years before eruption, continuously assimilating polyhedral olivine, and the melt evolved to a lower MgO composition. The melt became saturated in volatiles, and over-pressurisation of the shallow chamber lead to the onset of eruption. The platy cores nucleated and the melt degassed during ascent and upon emplacement at the surface. This degassing rapidly undercooled the melt, and the platy cores grew into the platy morphology. Those in the crust grew in situ and remain unzoned, whereas those in the lava core remained hot, acquired a rim of more evolved composition and diffused until the flow sufficiently cooled. During ascent, the polyhedral olivines acquired quenched rim overgrowths and Upon eruption the polyhedral olivines continued to diffuse in the lava transport system until the lava flow sufficiently cooled.

812x719mm (600 x 600 DPI)

Table 1: Moinui matrix glass compositions (oxide wt. %)

Glass	SiO_2	TiO_2	Al_2O_3	Cr_2O_3	FeO	NiO	MnO	MgO	CaO	Na_2O	K_2O	P_2O_5	Total	Mg#
M3T2 Glass1	52.65	2.30	13.72	0.05	9.38	0.03	0.15	6.65	10.74	2.36	0.37	0.21	98.62	0.56
M3T2 Glass2	53.49	2.34	13.56	0.04	9.52	0.02	0.15	6.80	10.79	2.34	0.39	0.23	99.68	0.56
M3T2 Glass3	52.52	2.31	13.59	0.06	9.43	0.02	0.14	6.70	10.70	2.46	0.37	0.19	98.50	0.56
M3T2 Glass4	52.88	2.36	13.93	0.03	9.54	0.02	0.17	6.68	10.66	2.49	0.41	0.28	99.45	0.56
M3T2 Glass5	52.59	2.33	13.95	0.03	9.42	0.02	0.15	6.67	10.61	2.54	0.35	0.27	98.94	0.56
M3T2 Glass6	53.07	2.36	13.54	0.03	9.41	0.01	0.13	6.69	10.60	2.53	0.41	0.23	99.00	0.56
M3T2 Glass7	53.20	2.35	13.96	0.05	9.56	0.01	0.14	6.64	10.65	2.42	0.38	0.21	99.57	0.55
M3T2 Glass8	53.22	2.31	13.69	0.06	9.40	0.03	0.16	6.72	10.67	2.47	0.41	0.24	99.37	0.56
M3T2 Glass9	52.91	2.31	13.23	0.06	9.45	0.00	0.14	6.66	10.66	2.39	0.39	0.21	98.40	0.56
M3T2 Glass10	53.20	2.30	13.69	0.02	9.42	0.02	0.17	6.74	10.65	2.39	0.39	0.22	99.20	0.56

Select Moinui glass compositions (oxide wt. %) measured using the EPMA from the Moinui lava flow. The average MgO matrix glass compositions used for the thermometry is 6.72 wt. % (calculated from 40 analyses ($1\sigma = 0.06$)).

(double column)

Table 2: Moinui olivine compositions and timescales (in days) calculated using Mg-Fe diffusion modelling.

Sample	Olivine	Morphology	Traverse	Core (Fo)	Rim (Fo)	Timescale (days)	Uncert. (+ days)	Uncert. (- days)
M1C	A	Polyhedral	1	89	84	2778	3351	1505
	A	Polyhedral	2	89	83	2489	3003	1349
	B	Polyhedral	1	90	83	2414	2912	1308
	B	Polyhedral	2	90	84	709	855	384
	C	Polyhedral	1	90	84	992	1197	537
	C	Polyhedral	2	90	84	706	852	383
	3	Bladed	A	82	76	46	55	25
	3	Bladed	B	82	77	60	72	33
	6	Bladed	A	83	65	3	4	2
	8	Bladed	A	82	75	20	24	11
	A	Polyhedral	1	89	83	2147	2590	1163
	A	Polyhedral	2	89	84	1424	1718	772
	C	Polyhedral	1	90	81	216	261	117
	C	Polyhedral	2	90	84	183	221	99
	D	Polyhedral	1	90	83	596	719	323
	E	Polyhedral	1	90	83	150	181	81
	B	Polyhedral	1	89	84	647	781	351
	B	Polyhedral	2	89	84	1739	2098	942

	D	Polyhedral	1	90	84	93	112	50
	D	Polyhedral	2	90	84	108	130	59
	F	Polyhedral	1	89	83	2297	2771	1245
	F	Polyhedral	2	89	82	2713	3273	1470

	Olivine	Morphology	Traverse	Core (Fo)	Rim (Fo)	Timescale (days)	Error (+ days)	Error (- days)
M2C	4	Bladed	A	82	76	17	21	9
	4	Bladed	B	82	73	2	2	1
	7	Bladed	A	82	72	14	17	8
	8	Bladed	A	82	74	22	27	12
	C	Polyhedral	1	89	86	291	351	158
	C	Polyhedral	2	89	85	415	501	225
M3C	C	Polyhedral	4	89	83	147	177	80
	L	Polyhedral	1	89	83	3411	4115	1848
	3	Bladed	A	82	78	6	7	3
	3	Bladed	B	82	76	9	11	5
	5	Bladed	B	82	72	14	17	8
	6	Bladed	A	82	78	3	4	2
M1T	D	Polyhedral	1	88	82	3413	4117	1849

Moinui olivine compositions and calculated Mg-Fe diffusion timescales that are representative of the dataset. Sample abbreviations are the same as those described in the text. All timescales are modelled

using a single temperature 1167°C and fO_2 of NNO-1. The errors are calculated accounting for temperature uncertainties (10°C), as well as uncertainties associated with activation energy and D_0, as described in the text.

(double column)